**Revision 1**

# Libyan Desert Glass: new evidence for an extremely high-pressure-temperature impact event from nanostructural study

**Word count: 8257**

Elizaveta Kovaleva[1,2,*], Hassan Helmy[3], Said Belkacim[4,5], Anja Schreiber[2], Franziska D.H. Wilke[2], and Richard Wirth[2]

[1] Department of Earth Sciences, University of the Western Cape, Robert Sobukwe Road, 7535 Bellville, South Africa

[2] Helmholtz Centre Potsdam – GFZ German Research Centre for Geosciences, Telegrafenberg, D-14473 Potsdam, Germany

[3] Department of Geology, Minia University, 61519-Minia, Egypt

[4] LAGAGE Laboratory, Department of Geology, Faculty of Sciences, Ibn Zohr University, P.O. Box 28/S, 80 000, Agadir, Morocco

[5] Research Institute on Mines and Environment (RIME), Université du Québec en Abitibi-Témiscamingue, 445 Boul. Université, Rouyn-Noranda, QC J9X 5E4, Canada

[*] Corresponding author. *E-mail address*: ekovaleva@uwc.ac.za (E. Kovaleva)

## Abstract

The origin of Libyan Desert Glass (LDG) found in the western parts of Egypt close to the Libyan border is debatable in planetary science. Two major theories of its formation are currently competing: (i) melting by airburst and (ii) formation by impact-related melting. While mineralogical and textural evidence for a high-temperature event responsible for the LDG formation is abundant and convincing, minerals and textures indicating high shock pressure have been scarce. This paper provides a nanostructural study of the LDG, showing

new evidence of its high-pressure and high-temperature origin. We mainly focused on the investigation of Zr-bearing and phosphate aggregates enclosed within LDG. Micro- and nanostructural evidence obtained with transmission electron microscopy (TEM) are spherical inclusions of cubic, tetragonal, and orthorhombic (Pnma or OII) zirconia after zircon, which indicate high-pressure, high-temperature decomposition of zircon and possibly, melting of $ZrO_2$. Inclusions of amorphous silica and amorphous Al-phosphate with berlinite composition ($AlPO_4$) within mosaic whitlockite and monazite aggregates point at decomposition and melting of phosphates, which formed an emulsion with $SiO_2$ melt. The estimated temperature of the LDG melts was above 2750 °C, approaching the point of $SiO_2$ boiling. The variety of textures with different degrees of quenching immediately next to each other suggest an extreme thermal gradient that existed in LDG through radiation cooling. Additionally, the presence of quenched orthorhombic OII $ZrO_2$ provides direct evidence of high-pressure (> 13.5 GPa) conditions, confirming (ii) hypervelocity impact origin of the LDG.

**Keywords:** granular textures, transmission electron microscopy, zircon, phosphates, zirconium oxide, orthorhombic zirconia OII, cubic zirconia, immiscibility

## Introduction

Libyan Desert Glass (LDG) is an enigmatic rock formation known to geologists for almost 90 years, which origin is still debated. In the past, various processes were suggested for the origin of the LDG: such as fulgurite (Baker 1959), meteorite collision (Kleinmann 1968), hydrothermal sol-gel process (Jux 1983; Feller 1997), sedimentary origin (Feller 1997), and a lunar volcanic source (Futrell and O'Keefe 1997). However, the low water content in the LDG (Beran and Koeberl 1997) together with the chemical and isotopic traces of meteoritic component (e.g., Murali et al. 1997; Rocchia et al. 1996; Barrat et al. 1997; Giuli et al. 2003), suggest the meteorite-related origin. Currently, the formation of LDG is considered

to be related to a short-lived high-temperature extraterrestrial event, with two major formation hypotheses suggested: (i) high-temperature fusion of surface materials by a large 100 Mt-class airburst (Seebaugh and Strauss 1984; Wasson 2003; Boslough and Crawford 2008; Aboud 2009; Boslough 2014), and (ii) high-temperature (Barnes and Underwood 1976; Kleinmann et al. 2001; Greshake et al. 2010; Greshake et al. 2018) and/or high-pressure (Cavosie and Koeberl 2019) melting by a meteorite impact.

Arguments for (i) airburst-related melting were the absence of the related impact crater and shock effects in the LDG. These led to a suggestion that LDG might be a product of a low-altitude atmospheric airburst that caused a high-temperature fusion of surface material (Wasson 2003; Svetsov and Wasson 2007; Boslough and Crawford 2008).

Evidence for (ii) impact-related melting has been presented in a series of papers (Kleinmann 1968; Koeberl 1997, 2000; Pratesi et al. 2002; Greshake et al. 2010, 2018), where the LDG is suggested to be the product of a high-temperature impact process. The occurrence of lechatelierite, α- and β-cristobalite, mullite, and possible tridymite enclosed in silica glass matrix provides evidence for high-temperature impact conditions (e.g., Urey 1957; Barnes and Underwood 1976; Greshake et al. 2018; Cavosie et al. 2022). Lechatelierite and α-cristobalite indicate heating of the source rock to at least 1550 °C followed by rapid cooling (Greshake et al. 2010). The observed complete breakdown of euhedral zircon grains resulting in baddeleyite and silica glass pseudomorph also implies a high-temperature event with a temperature above 1676 °C (Kleinmann 1968; Horn et al. 1997). The appearance of partially molten rutile grains indicates temperatures locally exceeding 1800 °C (Greshake et al. 2018). Finally, the presence of an emulsion of immiscible silicate melts is the evidence of high quenching temperatures up to 2100 °C, limited only by the temperature of silica vaporization (Pratesi et al. 2002).

The evidence for the high-pressure deformation due to collision with a meteorite remained elusive. Some authors demonstrated planar deformation features in quartz from float breccia and in the basement rock outcrops (Kleinmann et al. 2001; Koeberl and Ferriere 2019), suggesting the potential presence of a deeply-eroded impact crater, but the direct relation to LDG was not established. The most recent discovery of granular neoblastic zircon in LDG (Cavosie and Koeberl 2019) supports the high-pressure impact origin of the LDG. In particular, the presence of granular zircon with certain textures and orientations was suggested to indicate not only high-temperature but also impact-induced high-pressure origin of the LDG (Cavosie and Koeberl 2019). The authors reported zircon grains that have been partially dissociated into zirconia (presently baddeleyite) but preserved cores of granular neoblastic zircon. While the decomposition of zircon rims proves the elevated temperature (T > 1687 °C, Timms et al. 2017), the granular cores should indicate shock pressure above 30 GPa, according to Cavosie and Koeberl (2019). Although the $ZrSiO_4$ high-pressure polymorph reidite was not directly observed, the authors concluded that the textural analyses of the cores show the transformation of zircon into reidite and back to zircon (e.g., Cavosie et al. 2018a). However, Kovaleva et al. (2021) more recently demonstrated that the granular neoblastic zircon is not necessarily a product of solid-state phase transitions but may point at the complete breakdown into oxides, their disequilibrium melting, and rapid crystallization of zircon granules at high-temperature conditions. Thus, the granular zircon from LDG might need a closer investigation to identify its nature (solid-state high-pressure transformation vs. breakdown into oxides, melting and crystallization from melt), while the high-pressure model for the LDG formation needs more direct evidence. To address these concerns, we used high-resolution transmission electron microscopy (TEM) method combined with scanning electron microscopy (SEM) and electron probe microanalyses (EPMA), as well as energy dispersive X-ray analyses (EDX).

Transmission electron microscopy (TEM) is a powerful tool that can be used to support geochronology interpretations, and unravel complicated histories of terrestrial and planetary materials (Gu et al. 2020; Keller et al. 2021), internal structures and textures of major and accessory mineral phases, etc. (Kusiak et al. 2018; Seydoux-Guillaume et al. 2018). In particular, it is widely used to study and interpret processes recorded in terrestrial impactites (e.g., Pratesi et al. 2002), Lunar breccias (Kaneko et al. 2015; Wentworth et al. 1999) and meteorites (e.g., Leroux and Cordier 2006). TEM allows looking at individual mineral grains and, for example, facilitated studying the rock-forming minerals from the Lunar samples (e.g., Khisina et al. 2011; Keller et al. 2021). At the same time, very few TEM studies were conducted on shocked accessory minerals derived from impactites (Leroux et al. 1999; Reimold et al. 2002; Cox et al. 2020), even though TEM is a key instrument in studying microstructures, phase transitions, nano-inclusions, and lattice defects indicative of a variety of impact conditions (Kovaleva et al. 2021).

Applicable to LDG specifically, the dark streaks in the LDG were investigated by TEM (Pratesi et al. 2002), revealing the presence of nm-scale amorphous Fe-rich silicate spherules enclosed within the silica-glass matrix. Such amorphous spherules resulted from emulsion between two immiscible silicate liquids with similar viscosities. Moreover, cristobalite-mullite intergrowths from LDG were studied by TEM by Greshake et al. (2018), who concluded that these mineral phases crystallized from high-temperature silica melts. Here we present a TEM study of the accessory mineral phases (mainly Zr-bearing phases and phosphates) found in LDG, showing the impact-related high-temperature and high-pressure nanostructural features.

## Geological setting and sample description

Libyan Desert Glass (LDG) is a naturally occurring glass found over several thousands of square kilometers in flat corridors between the Sahara sand dunes in the southwestern parts of Egypt and southeast Libya in the Great Sand Sea (Fig. 1a, b). Clayton and Spencer (1934) first described it as wind-eroded fragments of various shapes and masses with homogeneous and relatively pure (98 wt% $SiO_2$) composition (e.g., Barnes and Underwood 1976; Frischat et al. 1984; Barrat et al. 1997). Fragments are found on the surface and below the surface up to a depth of 2 m (Weeks et al. 1984). The glass fragments vary from colorless and light-yellow to brown-green and grey, from milky to perfectly transparent. Some of them reveal brown flow banding and elliptical air inclusions (e.g., Barnes and Underwood 1976; Weeks et al. 1984). Brown bands or "streaks" were shown to contain meteoritic component (e.g., Koeberl 1997; Giuli et al. 2003). Source material for the LDG was suggested to be an Oligocene-Miocene mature sandstone (Fröhlich et al. 2013), composed of quartz grains, coated with mixed clay minerals and Fe-Ti oxides, and accessory phases (e.g., Fudali 1981; Barrat et al. 1997). The age of the LDG is determined by fission-track studies as 28.5 ± 0.8 Ma (Gentner et al. 1969; Bigazzi and De Michele 1996, 1997). This age, however, is in conflict with the supposed Miocene age of the source material.

Two angular fragments (Fig. 1c) of LDG were collected at the border between Egypt and Libya and obtained by one of the authors. Because of the lack of exact GPS coordinates of the sampling site, we consider their origin as part of the large LDG strewn field (Fig. 1b). Barakat et al. (1997) investigated more than 40 sites from the Great Sand Sea and noted that most of the LDG fragments were found within two main accumulation zones that are part of the LDG strewn field. Further, the fragments were distributed by fluvial transport to the south from the source area, resulting in the low-density population secondary distribution areas (Jimenez-Martinez et al. 2015). Sample A is approximately 2.5 x 1.4 cm, and sample B is slightly larger (3 x 2 cm). Both samples have an irregular shape, and their smooth surface was

likely obtained by the abrasive action of sandblasting in the desert environment. Samples are glassy and yellow in color (Fig. 1c). Sample A is milky and less transparent than sample B, containing multiple diffuse inclusions and/or vesicles. Sample B is more transparent but is also vesiculated. Each fragment was cut into two pieces to access the fresh central part. A thick section was prepared from the central part of each sample. In the text, the label A and B associated with the FIB foil number refers to sample A or B, respectively.

## Methods

Two polished thick sections were characterized with scanning electron microscopy (SEM), electron probe microanalyses (EPMA) element mapping, and subsequently prepared by the focused ion beam (FIB) for transmission electron microscopy (TEM) investigation. In the present study, we focused on mineral inclusions such as $ZrSiO_4$, $ZrO_2$, and $SiO_2$ polymorphs, and phosphates. After polishing the thick sections for a second time to access the deeper internal parts of the sample, additional FIB foils were prepared and investigated with TEM.

### Scanning electron microscopy (SEM)

Overview images of the single mineral grains in the Libyan Desert Glass samples were acquired with a Helios G4 UC DualBeam system (FEI-Thermo Fisher). For that purpose, the Everhart Thornly (ET) and through-the-lens (TL) detectors were used in secondary electron imaging mode (SE) and backscattered electron mode (BSE). The acceleration voltage was set to 5 and 10 keV, respectively.

### Electron probe micro-analyzer (EPMA)

Element distribution maps of zircon grains enclosed in LDG matrix were performed on a JXA8530F+ electron microprobe with a five wavelength dispersive spectrometer (WDS) so that five elements can be semi-quantitatively mapped simultaneously. 20 kV accelerating voltage and 20 nA beam current were used, and stage or beam scan mode was applied depending on the size of the grains of interest in the glass. The dwell time for each pixel was 400 ms. EMPA analysis and element mapping using the X-ray intensities of Si, Zr, Pb, Y, Th, and U have been applied to the three selected Zr-rich inclusions in LDG before FIB foil preparation: B#6410; A#6408 and B#6411 (Fig. S1 in Supplementary Material).

Elements detected were Si (Kα-Line) and Zr (Lα -Line) with peak position and high-voltage (HV) search done on natural zircon standard on TAP and PETH diffracting crystals, respectively. For Pb and U ($M_\beta$-Lines) as well as Th ($M_\alpha$-Line), peaks were detected on pure metal standards using PETL and PETH diffracting crystals, whereas for Y ($L_\alpha$-line) measured on TAPL crystal, a YAG standard was used. Results of maps were reported in counts per second level.

**Focused ion beam (FIB) sample preparation**

The foils were prepared with a Helios G4 UC DualBeam (Thermo Fisher) device. First, the area of interest was protected with a Pt-stripe 20 x 2 x 2 µm in size. Rough milling occurred with an acceleration voltage of 30 kV and a beam current of 45 nA to 9.3 nA. The raw FIB lamella was lifted out by an Easylift-System and fixed to a 3 mm half-moon copper grid. Then the FIB section was thinned to approximately 120 nm at 30 kV using decreasing beam currents from 0.79 nA – 80 pA. In a final polishing step at 5 kV and 41 pA, the FIB lamella was thinned and cleaned to ca. 100 nm in thickness.

**Transmission electron microscopy (TEM)**

198 The FIB foils were investigated with a TECNAI G2 F20 X-twin transmission electron
199 microscope (TEM) equipped with a Gatan Imaging Filter (GIF), a Fishione high-angle
200 annular dark-field system, and an EDAX X-Ray analyzer with ultrathin window. The TEM
201 was operated at 200 kV with a field emission gun as an electron source. Adjacent to
202 conventional bright-field (BF) and dark-field (DF) imaging, electron diffraction was applied.
203 BF, DF, and high-resolution lattice fringe images were acquired as energy-filtered images,
204 applying a 20 eV window to the zero-loss peak. Simultaneously, EDX spectra can be acquired
205 from the studied phase using a very small spot size (down to < 10 nm, depending on the size
206 of the object investigated), thus focusing on the object of interest. The chemical composition
207 provides basic information about the phase studied.
208 Besides conventional electron diffraction patterns, we used diffraction patterns
209 calculated from high-resolution lattice fringe images applying a Fast Fourier Transformation
210 (FFT) algorithm. FFT patterns were used to manually identify phases, in particular the $ZrO_2$
211 polymorphs. This technique was utilized for nanocrystalline phases to minimize electron
212 irradiation damage. The acquisition time for high-resolution lattice fringe images (HREM)
213 can be as short as 0.2 seconds. The measured length of the different diffraction vectors
214 (reciprocal space) is transformed into $d_{hkl}$ lattice spacing in real space. Additionally, the
215 angles between the different vectors are measured. The observed d-spacing and the angles
216 between adjacent planes are compared with calculated d-spacing and angles based on data
217 from the literature (unit cell parameters) for the expected phase. The observed angles between
218 adjacent lattice planes should match the angles calculated based on structural data from
219 literature within an error of ± 1°. Finally, the diffraction pattern can be indexed, and together
220 with the chemical composition from EDS the phase is fully identified.
221
222 **Results**

**SEM images and overview of TEM foils**

In total, we identified with SEM 14 different zircon/$ZrO_2$ aggregates ranging in size from 4 to 30 μm for subsequent TEM investigation. One TEM-FIB foil was prepared from each pseudomorph domain. Aggregates are mostly elongated with the moderate aspect ratios of 2:3 to 1:2. The original idiomorphic shape of zircon crystals is mostly preserved, indicating that these aggregated replaced individual zircon grains (e.g., Cavosie and Koeberl 2019). Some aggregates appear pulled apart and are composed of separated fragments of zircon or $ZrO_2$ enclosed in the silicate glass matrix. Based on the phases that are composing the Zr-bearing aggregates, we subdivided them into three groups. Pseudomorph aggregates, representative of all three groups, were found in both samples. For example, the former zircon grain in foil A#6408 is completely transformed into $SiO_2$ and Zr-oxide aggregate (classified here as group 1), which is found in two detached fragments of different sizes (Figs. 2a; S1b). The same impression is imposed on an aggregate in sample A#6409, composed of fully recrystallized granular neoblastic zircon with multiple Zr-oxide nano-inclusions (group 3, Fig. 2b).

**Group 1.** It includes idiomorphic zircon grains that have been completely transformed into vermicular granules of – usually twinned – baddeleyite enclosed in $SiO_2$ glass. A typical example of group 1 is shown in Figure 3a. Individual round or globular baddeleyite crystals are completely separated from other crystals or sometimes form clusters in the amorphous $SiO_2$ matrix. Five FIB foils were prepared from grains of group 1: A#6408, B#6410, B#6382, B#6370, and B#6379.

**Group 2**. This group comprises originally idiomorphic and/or rounded zircon, separated into two domains with a gradational boundary. The two domains contain different mineral phases and show different textures (Fig. 3b). One domain is composed of fully recrystallized granular neoblastic zircon, with μm-sized euhedral zircon granules separated by

triple junctions. Zircon grains contain round nm-sized inclusions of Zr-oxide and amorphous $SiO_2$ (Fig. 3b, upper part). The other domain is composed of vermicular Zr-oxide (baddeleyite) grains separated from each other by silicate glass (Fig. 3b, lower part). Baddeleyite is characterized by intense twinning and rounded grain shapes. The transition zone between two domains is usually a few tens of nanometers thick and presented by zircon rims enclosing baddeleyite cores. Three FIB foils were prepared from grains of group 2: A#6376, B#6381, and B#6371.

**Group 3**. This includes originally idiomorphic zircon that has been completely recrystallized to granular neoblastic texture. Grains from group 3 form zircon polycrystalline aggregates with nm-sized inclusions of Zr-oxide (bright) and amorphous $SiO_2$ glass (dark) enclosed in individual zircon crystals/granules or between them (Fig. 3c). The size of Zr-oxide (baddeleyite) inclusions ranges from 50 to 500 nm. Amorphous $SiO_2$ inclusions are usually less than 150 nm in size. The interface of the zircon aggregate with the host $SiO_2$ glass is irregular on a sub-μm scale. This type of zircon is documented in six FIB foils: A#6368, A#6367, A#6377, A#6409, B#6380, and B#6411.

Apart from zircon/former zircon, we found inclusions of α-cristobalite (FIB foil B#6373), Ca-phosphate phase whitlockite with amorphous Al-phosphate inclusions with berlinite composition (FIB foil A#6366), whitlockite with $SiO_2$ glass inclusions (FIB foil A#6378), and monazite with $SiO_2$ glass inclusions (FIB foil B#6499). Whitlockite and monazite grains are round or elliptical, ranging in diameter from 5 to 10 μm with numerous round inclusions of nm-size. In addition, two FIB foils cut from the glass matrix were investigated. Thus, in total, twenty FIB foils were investigated in this study.

**EPMA element distribution mapping**

In the three obtained EPMA maps, minor concentrations of Pb (< 10 counts per second – cps), Y (700 – 350 cps), Th (≤ 50 cps), and U (< 50 cps) were detected. Concentration changes cannot be tracked here. Apart from Zr and Si with intensities > 10 000 counts per second (cps), Y heterogeneities are detectable due to the broader range and generally higher intensities of ≤ 700 cps. In contrast, Pb is almost absent with intensities of ≤ 10 cps as mentioned above. U and Th show similar intensities, but U is mostly homogeneous while Th reveals patchy distribution (see Fig. S1). In grains of group 1 (Fig. S1a-b), higher intensities of Y and Th and lower Si are attributed to baddeleyite, in which the Zr intensity is also high (Fig. S1a). The Si-dominated Libyan Desert Glass A and B samples are homogeneous for Si, Mg, Ca, and Fe. Minor Al-rich inclusions were detected by EDX.

**Detailed TEM observations**

This subsection presents the detailed micro- and nanostructural observations of inclusions in LDG (zircon, former zircon, and phosphates, as well as α-cristobalite). The presentation of each grain starts with a brief description of the grain as it is visible in the SEM image before FIB sample preparation, where the cross-sectional line indicates the position of the extracted FIB foil. Each SEM image is shown with the corresponding TEM high-angle annular dark-field (HAADF) image as an overview image. These two images together provide a three-dimensional impression of the object. $ZrO_2$ polymorphs, were identified using d-spacing and angles between adjacent lattice planes derived from the FFT patterns (Table 1).

**Group 1 (former zircon completely dissociated into baddeleyite and $SiO_2$).** Figure 4a displays a BSE image of granular Zr-oxide in an amorphous $SiO_2$ matrix (B#6410). The FIB foil (Fig. 4b) is cut normal to the thin section surface and shows Zr-oxide grains (bright) in an amorphous $SiO_2$ matrix (dark). Both images (Fig. 4a-b) display (sub)round granules of

297 Zr-oxide with a few that are connected, forming sintering necks. Additionally, completely
298 isolated spherical grains of Zr-oxide are observed in the $SiO_2$ matrix (Fig. 4b-d). The larger
299 Zr-oxide grains (> 150 nm) show polysynthetic twinning, thus identifying them as baddeleyite
300 with the monoclinic crystal structure (Fig. 4b,d). Smaller isolated round grains (< 150 nm) are
301 not twinned and have a cubic crystal structure, as evidenced by their FFT diffraction patterns
302 (Fig. 4c,d; insets). Cubic Zr-oxide nano-grains isolated in the $SiO_2$ glass matrix have been
303 confirmed in foils B#6370, B#6382, B#6410.

304 **Group 2 (zircon composed of two zones: polycrystalline zircon and baddeleyite).**
305 An example from this group is shown in Figure 5a-b, FIB foil A#6376, and represents an
306 originally idiomorphic former zircon crystal ca. 10 x 7 μm in size. The left part of this grain is
307 composed of round or elongate vermicular baddeleyite grains, usually detached from each
308 other, twinned and embedded in $SiO_2$ glass. The intercalating $SiO_2$ glass contains minor
309 concentrations of Al and P (Fig. 5c). The right part of the grain consists of polycrystalline
310 zircon composed of granules that are usually < 1 μm in size. While the baddeleyite domain
311 has isolated granules "floating" in the silica glass, the polycrystalline zircon part contains few
312 inclusions of $SiO_2$ along the boundaries between zircon granules (Fig. 5d). Individual zircon
313 granules have low dislocation density, few internal low-angle grain boundaries, and common
314 120° angles at triple junctions, thus indicating an equilibrium texture (Fig. 6a). Zircon shows
315 clear diffraction contrast in TEM bright-field images (Fig. 6a), unlike the patchy or mottled
316 contrast typical for irradiation-damaged metamict zircon (e.g., Capitani et al., 2000). Some
317 zircon granules contain nm-sized (10-50 nm) inclusions of $ZrO_2$ and amorphous $SiO_2$ (Fig. 6a,
318 arrows). Very small (< 15 nm in diameter) and round inclusions of Zr-oxide in zircon have a
319 tetragonal crystal structure (Fig. 6b). No orientation relationships between tetragonal Zr-oxide
320 inclusions and the host zircon granules are observed.

The transition between zircon-rich and baddeleyite-rich domains of group 2 aggregates is gradational and contains zoned granules composed of baddeleyite cores and zircon rims surrounded by the $SiO_2$ glass (Figs. 5d; 6c). The thickness of zircon rims in these granules ranges from 30 to 50 nm. No orientation relationships between baddeleyite cores and zircon rims were documented (c.f. diffraction patterns in Fig. 6d). Gaps are visible between the zircon rim and the baddeleyite core in the center of Figure 6c, indicating a lack of connectivity, possibly, due to a different thermal contraction during the cooling of these phases and/or differences in volume. Similar effect is observed in Figure 10a between the whitlockite and host silica glass.

**Group 3 (granular neoblastic zircon).** The SEM image (B#6411) in Figure 7a shows a representative example of this group. The originally (sub)idiomorphic zircon grain is presently polycrystalline, comprising multiple sub-μm crystals or granules of zircon (Fig. 7b). In literature, such texture is referred to as "granular neoblastic zircon" (Cavosie et al. 2018a; Cavosie and Koeberl 2019). The interface between zircon and $SiO_2$ matrix is irregular even at low magnification. The central part of the crystal contains multiple bright inclusions of Zr-oxide and dark inclusions of amorphous $SiO_2$ (Fig. 7a-b). Approximately 1 μm away from the main zircon mass, in the amorphous $SiO_2$ matrix, several elongated drop-shaped zircon aggregates are visible (Fig. 7b, arrows; 7c). Amongst these elongated neoblastic zircon granules, isolated nm-sized spherical Zr-oxide inclusions are seen (Fig. 7c). Their cubic structure is derived from an FFT diffraction pattern (Fig. 7c, inset).

The bright-field image Figure 8a shows a typical densely-packed microstructure of the main mass of the granular neoblastic zircon. The grain size is usually less than 1 μm, and grains are in clusters with different orientations (Fig. 8a). The individual crystals display clear diffraction contrast without a typical patchy contrast due to irradiation damage of metamict zircon (Fig. 8a). Dislocation density is very low, with only a few low-angle grain boundaries

346 are visible. Frequent 120° angles at triple junctions suggest equilibrium conditions during
347 crystal growth. Many of the individual zircon crystals contain dark nano-inclusions of less
348 than 20 nm in diameter (Fig. 8b). These inclusions are Zr-oxide spheres with a cubic crystal
349 structure (Fig. 8c). The diffraction pattern shows that there is no orientation relationship
350 between zircon and enclosed Zr-oxide. In addition to the Zr-oxide inclusions, frequent
351 amorphous $SiO_2$ inclusions are present, most often located at triple junctions between zircon
352 granules. Round inclusions of $SiO_2$ a few tens of nanometers in diameter also occur inside
353 zircon granules.

354 In all six investigated FIB foils of zircon from group 3, small (< 50 nm) round
355 inclusions of cubic Zr-oxide and larger (< 50 nm) round inclusions of tetragonal Zr-oxide are
356 observed in zircon. In one sample (foil A#6409), spherical inclusions of Zr-oxide with
357 orthorhombic crystal structure have been identified enclosed with zircon granules (Fig. 8b;
358 Table 2).

359 **Phosphates.** The elliptical inclusion of whitlockite (Fig. 9a-b, FIB foil A#6378) is ca.
360 10 μm in diameter. The inclusion is composed of mosaic whitlockite with multiple nm-sized
361 pores. The whitlockite phase was confirmed from its diffraction pattern (FFT) (Fig. 9d) and is
362 checked by simulating the diffraction pattern using the experimental indexing of the pattern
363 and the resulting zone axis orientation. The simulated diffraction pattern matched the
364 experimental diffraction pattern. The individual whitlockite subgrains are nm-sized and have
365 irregular shapes. The pores appeared empty, possibly due to FIB milling, and must have been
366 initially filled with fluid or gas. Additionally, multiple perfectly spherical inclusions of
367 whitlockite occur in the amorphous $SiO_2$ matrix, ranging from tens of nm to 300 nm in
368 diameter. EDX analyses of larger mosaic whitlockite, as well as whitlockite in smaller round
369 inclusions, show minor concentrations of Y and F, in addition to major Ca, P, and O (Fig. 9c).

Another mosaic whitlockite-bearing inclusion was found in foil A#6366, containing many inclusions of an amorphous Al-phosphate with the chemical composition of berlinite and < 200 nm in diameter (Fig. 10 a-b). Berlinite is very sensitive to electron irradiation so its unknown whether it was amorphous initially, or if it was crystalline and became amorphous as a result of TEM imaging. Whitlockite was confirmed by diffraction data (Fig. 10d, left). Note the gap between the whitlockite aggregate and the glass matrix on the right-hand side. Smaller spherical berlinite-free inclusions of whitlockite are enclosed within the $SiO_2$ matrix. The diameter of these circular inclusions ranges from tens of nm to hundreds of nm (Fig. 10a).

Monazite inclusion (FIB foil B#6499) has a sub-round shape and is hosted by an amorphous $SiO_2$ glass matrix (Fig. 11). The monazite phase was identified from diffraction data and chemical composition: it contains Ce, La, Th, U, and Y as major constituents (Fig. 11d-e). The peaks of these elements are present in several EDX spectra of the studied monazite (Fig. 11e). Dark $SiO_2$ glass inclusions are mostly randomly distributed within monazite and have variable sizes (few nanometers up to hundreds nanometers; Fig. 11a-c). Some larger inclusions contain Al and P in low concentration, possibly pointing at the presence of berlinite. Monazite grain contains multiple dislocations frequently pinned by round or elliptical $SiO_2$ inclusions (Fig. 11c).

**Cristobalite and glass matrix.** Locally, the silica matrix of the LDG contains volumes crystallized as intensely twinned cristobalite (Fig. 12). Such twinned cristobalite has already been reported in other studies of LDG (Greshake et al. 2010, 2018). We also investigated the glass matrix (FIB foils A#6374, A#6365). The $SiO_2$ glass is predominantly composed of Si, oxygen and minor concentrations of Al, which is merely above the EDX detection limit (approx. 0.2 at%) and matches the composition reported earlier (Greshake et al. 2010, 2018). The glass is homogeneous without any inclusions within the area of the analyzed FIB foils (15 μm x 10 μm).

## Discussion

### Airburst or impact?

Two main models were previously suggested for the formation of LDG. Airburst (i) would involve high-temperature fusion of surface material at relatively low pressures below 10 kPa (e.g., Brown et al. 2013). The model of airburst was proposed and discussed in several publications (Wasson 2003; Boslough and Crawford 2008) and was rejected as unrealistic, for example, by Cavosie and Koeberl (2019), who noted that massive 100 Mt-class airbursts are not documented in the terrestrial record elsewhere.

In contrast, meteorite impact (ii) would have involved both high-temperature and high-pressure conditions of target rocks deformation. This model is favored by several researchers (Kleinmann 1968; Koeberl 1997, 2000; Pratesi et al. 2002), but the indisputable evidence for shock pressure remained elusive.

High-temperature processes observed in LDG, such as dissociation of zircon to zirconium oxide and silica, formation of α- and β-cristobalite and mullite, etc. are in agreement with both (i) low-altitude airburst and (ii) impact process (El Goresy 1965; Kleinmann 1968; Greshake et al. 2018; Cavosie et al. 2022) and thus are not able to resolve the existing argument. The suggested former presence of reidite in LDG (in the form of granular zircon) would allow shock pressures above 30 GPa, favoring the impact model (Cavosie and Koeberl 2019). However, we observed no evidence for the solid-state phase transition between zircon and reidite in our samples of LDG. The suggested genetic relationships between zircon-reidite phase transformation and granular zircon has been recently shown as non-unique interpretation (Kovaleva et al. 2021) and other mechanisms other that reidite reversion exist to produce granular recrystallized zircon during shock

(Wittmann et al., 2006). Hence, more evidence for high-pressure LDG formation model is needed.

**High-pressure markers**

Our observations provide arguments supporting both high-pressure and high-temperature processes related to LDG formation. The nanocrystalline $ZrO_2$ with orthorhombic Pnma cotunnite ($PbCl_2$) structure, also known as Ortho-II or OII (e.g., Ohtaka et al. 1991; Haines et al. 1995; Bouvier et al. 2000), was identified in zircon from FIB foil A#6409 (Fig. 8b) and is a high-pressure phase. Its pressure stability field lies between 12.5-24 GPa, and it is stable under temperature up to 1800 °C (Liu 1980; Block et al. 1985; Ohtaka et al. 1991, 2001; Haines et al. 1995). Orthorhombic $ZrO_2$ is metastable under atmospheric pressure (Suyama et al. 1985) and is considered to be non-quenchable at ambient conditions. It can, however, be preserved in ultrafine grains only, by quenching at high temperature and high-pressure experimental conditions (Block et al. 1985; Ohtaka et al. 1991; Bouvier et al. 2000).

Darling et al. (2016) suggested that high-pressure phases of $ZrO_2$ can be preserved as the nanometer-size lattice fragments or inclusions in natural impactites. Previously, possible presence of the OII $ZrO_2$ polymorph was reported by Wittmann et al. (2006), who documented weak Raman bands of this phase in former zircon aggregates, partially decomposed to $ZrO_2$. OII polymorph was suggested to represent evidence of high-pressure decomposition, and to be preserved in rapidly-quenched impact melt domains from Ries and Chicxulub craters. However, due to the low spectral resolution, the full Raman bands characteristics of this phase was not possible (Wittmann et al. 2006). Former presence of orthorhombic $ZrO_2$ polymorph was reconstructed from Sudbury polycrystalline baddeleyite grains using the method of phase heritage reconstruction (White et al. 2018), and was also suggested to be present in shergottite (Martian meteorite, Darling et al. 2016). Hence, the

presence of such $ZrO_2$ polymorph in impact-related rocks was expected and finding it was only a matter of time and methods.

Our report of the high-pressure orthorhombic phase of $ZrO_2$ might be the first direct observation of the orthorhombic OII polymorph of $ZrO_2$ in nature (e.g., White et al. 2018). On the other hand, our finding of the OII phase of Zr-oxide in GDL samples is a direct evidence of its high-pressure impact origin.

**High-temperature markers**

The observed phases of $ZrO_2$ (specifically cubic, tetragonal, and monoclinic) and phosphates, as well as microstructures provide a series of temperature markers for our samples. However, we assume that the implied reactions had occurred in non-equilibrium conditions, and the observed melting was incipient and non-congruent while crystallization was non-equilibrium; therefore, cited temperatures derived from equilibrium phase diagrams are used as approximations only.

The appearance of rounded baddeleyite aggregates in textures of groups 1 and 2 (Fig. 3) and the presence of $ZrO_2$ and $SiO_2$ inclusions in zircon granules from groups 2 and 3 (Figs. 6a, 7a, 8a) point at the presence of two phases – Zr-oxide (in solid or molten stage) and silica melt, coexisting as an emulsion. If Zr-oxide was in a molten state, the temperature within the LDG must have exceeded the melting temperature of zirconia, which is 2700-2750 °C under equilibrium conditions (Nassau 1981; Kaiser et al. 2008). Moreover, the immiscibility of two liquids in the $ZrO_2$-$SiO_2$ system exists under conditions of congruent melting in the interval of ca. 2250-2700 °C (Kaiser et al. 2008; Kwon and Jung 2017). The cited temperatures closely approach the vaporization temperature of the host $SiO_2$, which is estimated at 2866-2884 °C (Schnurre et al. 2004; Melosh 2007). Local boiling of $SiO_2$ material can explain vesiculated texture observed in many samples of LDG (Fig. 1c). It should be noted that the emulsion

469 textures in LDG were reported before, being interpreted as a result of the silicate-silicate
470 liquid immiscibility (Pratesi et al. 2002). Silica glass would have been highly viscous in such
471 emulsions (Diemer 1997), mostly preserving the coexisting melts in a single pool with a few
472 exceptions, where the aggregates of Zr-bearing pools are visibly separated (e.g., Fig. 2).

473 The coexistence of Zr-oxide nano-spheres with cubic and tetragonal structure with
474 twinned baddeleyite grains of larger size (Fig. 4) indicate that Zr-oxide had originally
475 crystallized in cubic structure and transformed into tetragonal and finally twinned monoclinic
476 structure during cooling (e.g., Cayron et al. 2010). It should be mentioned that apart from
477 direct observation of relict cubic and tetragonal phases (Kovaleva et al. 2021; this paper),
478 another method to identify precursor phases for baddeleyite is a phase-heritage reconstruction
479 approach using electron backscatter diffraction (EBSD) mapping. Specific crystallographic
480 relationships between grains in polycrystalline baddeleyite possibly point at the phase
481 transition from cubic to tetragonal and further to monoclinic or orthorhombic $ZrO_2$ (Timms et
482 al. 2017; White et al. 2018). Although we have not employed EBSD technique in our study,
483 we obtained the same conclusions by direct observations of these phases in nano-particles.

484 In $ZrO_2$ grains larger than 150 nm, phase transformation of cubic zirconia to tetragonal
485 zirconia should have taken place at 2370 °C (Subbarao 1981; Block et al. 1985). Tetragonal
486 structure had been stable in the temperature interval of 2370°C – 1687°C (e.g., Kaiser et al.
487 2008). The intense polysynthetic twinning in baddeleyite is a common feature that results
488 from phase transformation from tetragonal to monoclinic structure (McCullough and
489 Trueblood 1959), and is described in literature on ceramic materials (Jin 2005; Chevalier et al.
490 2009). The cubic and tetragonal crystal structures were preserved in nano-spheres of Zr-oxide
491 of < 150 nm in diameter only, where the nanometer size of the spheres prevents them from
492 phase transformation (Kovaleva et al. 2021). Such behavior of nanocrystalline material is
493 known from nanocrystalline Fe, which transforms from α-iron (bcc) into γ-iron (fcc) upon

494 heating above 912°C. The reverse phase transformation occurs during subsequent cooling, but
495 the high-temperature fcc structure is preserved in nanocrystalline Fe grains (Gleiter 1989).

496 We also observed an inclusion of monazite in amorphous silica. No lamellae or
497 polysynthetic twins were observed in monazite, which could have been attributed to the
498 former existence of a shock-produced high-pressure (La,Ce,Th)$PO_4$ polymorph. Such
499 polymorph was inferred from systematically oriented lamellae in monazite from the
500 Nördlinger Ries Crater in Germany, and Haughton Dome, Nunavut in Canada (Erickson et al.
501 2019). In contrast, the spherical shape of monazite inclusion in our sample indicates that
502 molten droplet(s) of phosphate melt has been enclosed in a silica melt pool. Complete melting
503 is further supported by the presence of small – up to a few tens of nanometers – amorphous
504 $SiO_2$ spherical inclusions in monazite (Fig. 11). The evidence for the monazite in situ melting
505 was documented in LDG previously (Fröhlich et al. 2013) and microstructures indicate
506 unmixing of two co-existing melts: $SiO_2$ melt and phosphorus-rich melt. The melting point of
507 natural monazite is in the range of 1900 – 2100°C in equilibrium conditions (e.g., 2057°C ±
508 40 °C, Hikichi and Nomura 2005), which provides the next temperature marker for our
509 samples.

510 Furthermore, numerous spherical or drop-like inclusions of other phosphates
511 (whitlockite and amorphous berlinite) in the amorphous silica matrix have been detected.
512 Crystalline berlinite has the structure of quartz and is analogues to it, and both $SiO_2$ and
513 $AlPO_4$ phases are present as amorphous material in our samples. However, it is not clear if
514 berlinite was amorphous initially or became amorphous as a result of electron beam treatment.
515 The size of these inclusions is in the range of tens of nanometers up to several micrometers.
516 Like monazite, microstructures and textures in whitlockite indicate the complete melting of
517 this phosphate and its existence in emulsion with silica melt (Figs. 9b; 10a). The melting
518 temperature of whitlockite is approximately 1400°C (McCubbin et al. 2017).

519

520 **Zircon and former zircon textures observed in LDG**

521 According to Cavosie and Koeberl (2019), three populations of zircon/former zircon
522 occur within samples of LDG: (1) zircon grains with granular neoblastic domains interpreted
523 as "the oldest generation of zircon"; (2) zircon grains wholly dissociated to baddeleyite and
524 $SiO_2$; and (3) "dissociated grains that back-reacted with melt to form the second generation of
525 neoblastic zircon" interpreted as the youngest generation of zircon. Texturally, population (1)
526 corresponds to our group 3; population (2) corresponds to our group 1, and population (3)
527 likely corresponds to our group 2. Note that we did not use the nomenclature suggested by
528 Cavosie and Koeberl (2019) because we suggest a different formation sequence for the
529 zircon/former zircon textures observed in LDG based on nano-structural observations.
530 According to our data, three groups/generations of zircon represent snapshots of the same
531 evolutionary path with different cooling histories, where completely dissociated into $ZrO_2$
532 grains (group 1) is the earliest generation, and the granular neoblastic zircon grains (group 3)
533 is the latest crystallized grains/aggregates.

534 **Group 1.** This population (population 2 by Cavosie and Koeberl 2019) represents the
535 immediate quenching of LDG glass after the impact-related pressure-temperature pulse.
536 Presently, the former zircon grains have been completely transformed into baddeleyite with
537 intensely twinned vermicular crystals surrounded by $SiO_2$ glass (Fig. 4b, d). Similar textures
538 have been reported from LDG before (Kleinmann 1968; Fröhlich et al. 2013; Cavosie and
539 Koeberl 2019), as well as from impact glasses, tectites, melts and suevites (e.g., El Goresy
540 1965; Wittmann et al. 2006; Tolometti et al. 2022), and also fulgurites – the products of
541 lightning strikes (Kenny and Pasek 2021). Such textures are consistently explained as zircon
542 breakdown into tetragonal $ZrO_2$ and cristobalite/$SiO_2$ melt that at ambient pressure happens at
543 temperatures over 1673 ± 10 °C with eutectic temperature of 1687 ± 10 °C (e.g., Kaiser et al.

544 2008). In experiments, these dissociation textures were produced by heating of zircon at
545 1600-1700°C and its resulting decomposition into columnar or dendritic particles of $ZrO_2$
546 coated by a film of amorphous $SiO_2$ phase (Kaiser et al. 2008).

547 Our TEM observations not only show the dissociation of zircon into $ZrO_2$ and $SiO_2$,
548 but, at least locally, the complete melting of Zr-oxide and silica, thus indicating temperatures
549 over 2750 °C (see section 5.3). The argument for the melting of Zr-oxide is the round shape
550 of $ZrO_2$ crystals both as inclusions in newly crystallized zircon (e.g., Fig. 8c), and spheres
551 isolated in $SiO_2$ glass (Figs. 4c-d; 7c). We suppose that liquid Zr-oxide and silica melt have
552 segregated, thus forming immiscible emulsion, resulting in quenched droplets of Zr-oxide
553 melt within silica melt.

554 There are no reliable data on Zr saturation in silica melt at such high temperatures. It
555 can be expected from the existing data that, providing sufficient time, a large fraction of Zr
556 dissolved in silica at a temperature below the immiscibility field (< ca. 2250 °C) because
557 dissolution of Zr is temperature-dependent (Watson and Harrison 1983; Boehnke et al. 2013;
558 Gervasoni et al. 2016; Shao et al. 2020). For example, in a recent experimental study, in a
559 temperature range of 1150-1500 °C, the concentration of Zr in silicate glasses varied from
560 0.454 up to 6.137 wt% (Borisov and Aranovich 2019). Thus, local melting and crystallization
561 of $ZrO_2$ within the sampled LDG must have happened instantaneously so that only a
562 negligible fraction of $ZrO_2$ from group 1 aggregates was dissolved in $SiO_2$ as indicated by the
563 composition of the host silica glass. Locally, zircon could have decomposed into solid $ZrO_2$
564 and liquid $SiO_2$, as predicted to happen above 1687 ± 10 °C. Here again it must be
565 emphasized that shock (incongruent) melting is caused by non-equilibrium conditions within
566 different microenvironments.

567 Our observations of group 1 prove rapid heating and decomposition or partial melting
568 of zircon followed by rapid melting of Zr-oxide, which, at least locally, forms droplets of

569 oxide melt in silica melt. Because of the extremely short time of the heating event, re-
570 equilibration was impossible, and Zr mostly remained contained in Zr-oxide melt/solid.
571 During cooling, Zr-oxide crystallizes first with a cubic structure, which is preserved only in
572 the nm-sized inclusions. The larger droplets of cubic zirconia (> 150 nm) experienced a phase
573 transformation into a tetragonal and subsequently stable monoclinic structure.

574 Unlike common textures documented in Ries and Aouelloul glasses (El Goresy 1965),
575 we did not observe extensive baddeleyite schlieren around the decomposed zircons that would
576 be indicative of glass flow. We documented only minor pull-apart textures (Fig. 2), which are
577 not as extensive as in cited glasses. Hence, the host LDG solidified very rapidly with
578 minimum displacement, confirming the fast quenching.

579 **Group 2.** This group (population 3 by Cavosie and Koeberl 2019) represents initially
580 idiomorphic zircon grains that are now composed of two domains: dense polycrystalline
581 zircon and baddeleyite granules separated by areas of $SiO_2$ glass (Fig. 5a-b). In the
582 transitional zone between two domains, we observed granules with $ZrO_2$ cores and thin zircon
583 rims (Figs. 5d; 6c). The pre-existing zircon grains have been dissociated into $ZrO_2$, which was
584 likely partly molten, as seen from the shapes of baddeleyite grains and presence on micro- and
585 nano-inclusions of $ZrO_2$ and $SiO_2$ within the granular zircon domain. Just as for group 1, the
586 observed textures indicate the presence of two immiscible melts, $SiO_2$ and $ZrO_2$, at a certain
587 stage of LDG evolution. One part of the $ZrO_2$ pool cooled down and was quenched rapidly,
588 thus demonstrating the same textures as in group 1.

589 However, the transitional zone experienced annealing or was not immediately
590 quenched, causing a diffusion reaction between $ZrO_2$ and $SiO_2$ components of the system,
591 which backreacted forming $ZrSiO_4$ rims around the $ZrO_2$ (Fig. 6c). Such textures, with $ZrO_2$
592 cores and zircon rims enclosed in $SiO_2$ matrix, are observed in natural impact glasses (e.g.,
593 Tolometti et al. 2022), and in experiments where $ZrSiO_4$ was decomposed by annealing and

then quenched, suppressing the reverse reaction (e.g., Curtis and Sowman 1953; Kaiser et al. 2008). Upon further experimental annealing at 1500°C, $ZrO_2$ is almost entirely consumed, leaving behind small round particles embedded in zircon, while the nucleating zircon grains start sintering (Kaiser et al. 2008).

The domain with granular zircon cooled down even slower, or were annealed, allowing most of the Zr to dissolve in silica and crystallize as granular zircon. The average grain size of newly grown zircon is < 1μm, and nanometer-sized spherical inclusions of amorphous silica are common. The Zr-oxide nano-inclusions in zircon occasionally preserve a tetragonal structure, indicating temperature drop from 2750 °C down to 2370 °C, the temperature of tetragonal zirconia stability.

**Group 3.** Group 3 (population 1 by Cavosie and Koeberl 2019) represents granular zircon, with granules containing inclusions of Zr-oxide and amorphous silica (Fig. 7a-b). Similar neoblastic zircon aggregates were reported from impact glasses and melts (e.g., Wittmann et al. 2006, 2009; Cavosie et al. 2018a; Hauser et al. 2019), as well as tektites (Cavosie et al. 2018b), and their presence suggests the possibility of dating of the shock event (e.g., Kenny et al. 2017, 2019; Erickson et al. 2020; Hauser et al. 2019).

Witmann et al. (2006) noted that granular zircon aggregates could result from: (i) a back-reaction of $ZrO_2$ with $SiO_2$ during evolution of impact melts, (ii) by reversion of reidite to zircon but without decomposition to $ZrO_2$, or (iii) by heating and crystallization of the diaplectic zircon glass. All three mechanisms are the result of thermal annealing. According to the mechanism (i) suggested by Wittmann et al. (2006), based on the ubiquitous presence of $ZrO_2$ particles, we conclude that this textural group is the last member of the same evolutionary path recorded by groups 1 and 2, but represents a longer and slower cooling history accompanied by annealing. Thus, most of the $ZrO_2$ back-reacted with $SiO_2$ to form polycrystalline zircon aggregates. The abundance of round $ZrO_2$ and $SiO_2$ inclusions within

619 the zircon granules might indicate the former melt presence, and cubic and orthorhombic
620 $ZrO_2$ nano-inclusions provide high-temperature and high-pressure markers accordingly.
621 Zircon rims documented around $ZrO_2$ grains represent a snapshot of this process (Figs. 5d, 6c).
622 Similar crystallization into granular zircon has been reported recently within a sample from
623 the Vredefort impact structure (Kovaleva et al. 2021).

624 Crystallization of zircon granules due to dissolution/backreaction of isolated grains of
625 $ZrO_2$ (Fig. 4a-b) might explain the granular nature of zircon aggregates, i.e., each zircon
626 granule nucleates around a single $ZrO_2$ droplet. The presence and elongated tear-drop shapes
627 of isolated zircon grains in the $SiO_2$ matrix (Fig. 7c) closely resemble the isolated baddeleyite
628 crystals from group 1 aggregates (Fig. 3a), suggesting their genetic relationships.

629 Textural group 3 cannot represent the oldest group suggested earlier. The presence of
630 $ZrO_2$ and $SiO_2$ inclusions in zircon granules even in the center of an aggregate indicate that
631 these phases existed before the observed zircon and were captured during its growth (Fig. 8a-
632 b). Thus, aggregates from group 3 went through the entire cycle: zircon –> $ZrO_2$ + $SiO_2$ –>
633 zircon. Transition zones in group 2 clearly illustrate the direction of this reaction (Fig. 6c).
634 We do not exclude that before decomposition to oxides, zircon was transformed to reidite
635 (Cavosie and Koeberl 2019), however, there are no preserved indicators.

636 Occasionally observed roughly systematic orientation of zircon granules (e.g., Cavosie
637 et al. 2018a; Cavosie and Koeberl 2019) in granular neoblastic zircon can be explained by
638 crystallographic control on newly-growing zircon granules of pre-existing $ZrO_2$ grains.
639 However, we did not observe any crystallographic relationships between $ZrO_2$ and newly
640 formed zircon granules in LDG, and the presence or absence of such relationships needs to be
641 investigated more closely. Another possible option is, for example, the surface energy effects
642 (e.g., growth twinning, parallel growth, synneusis, etc.; see Kovaleva et al. 2021), which
643 would be feasible in case of crystallization form melt. The high Si and low K, Na, and Ca

644 abundances in the host melt (Fig. 5c) and the general disequilibrium state of the system could
645 have allowed for zircon to crystallize at high temperatures within a partially liquid
646 environment. The compositional parameter of the host environment M = [(K + Na +
647 2Ca)/(Al*Si)], which, under static conditions, affects zircon crystallization temperature, is
648 rather high to increase the temperature of zircon nucleation (e.g., Harrison et al. 2007).

649 The presence of three types/groups of (former) zircon textures shows the difference in
650 cooling temperature and implies that the thermal gradient in LDG was extreme. This thermal
651 gradient produced various textures across the distance of just a few micrometers (Figs. 3b; 5),
652 which indicates that the heat loss of LDG during cooling was related mainly to radiation with
653 little convection or conduction. Further studies of thermal profiles and numerical modeling
654 would shed more light on the cooling processes in LDG.

655

656 **Implications**

657 The presented data of the TEM investigation of the LDG supports a high-temperature
658 event with a complete decomposition of zircon into $ZrO_2$ and $SiO_2$ and subsequent melting of
659 Zr oxide, implying a temperature exceeding 2750 °C, approaching the $SiO_2$ boiling
660 temperature. At these conditions, Zr oxide and silica formed solid/liquid or liquid/liquid
661 suspensions that subsequently were either quenched as an emulsion or dissolved in each other
662 upon slower cooling, back-reacting to form granular zircon. The microstructures observed in
663 three different groups of (former) zircon aggregates in LDG can be explained by a high-
664 temperature event and varying cooling rates conditioned by extreme thermal gradient within
665 the LDG. In addition, complete melting of phosphates whitlockite and monazite and the
666 presence of spherical inclusions of amorphous berlinite in one of the whitlockite aggregates
667 support the ultrahigh-temperature model of the LDG formation. The high-pressure nature of
668 the event is proved by the occurrence of quenched nano-inclusions of orthorhombic $ZrO_2$ – a

669 rare high-pressure polymorph and thus supports the high-pressure model proposed by Cavosie
670 and Koeberl (2019).

671 Our study demonstrates that the impact crater responsible for the LDG formation is
672 yet to be recognized and its cooling mechanism is to be modelled. On the other hand, it shows
673 thar there are other mechanisms for granular zircon formation other than a solid-state phase
674 transition to reidite and back to zircon and that such microstructures by itself indicate rather
675 shock-related high temperature events and not shock pressures. We emphasise the importance
676 of TEM studies in understanding of such complicated deformation features as shock-related
677 deformations in accessory minerals.

678

679 **Acknowledgments**

680 The Alexander von Humboldt Foundation has provided funding for this research to
681 E.K. We acknowledge anonymous reviewers and the editor for their constructive comments
682 and interesting discussion.

683

684 **Supplementary material**

685 **Figure S1.** Chemical maps of selected (former) zircon grains from the LDG; (**a**) and
686 (**b**) – grains group 1; (**c**) – grain group 3.

687

688 **References**

689 Abate, B., Koeberl, C., Kruger, F.J., and Underwood, J.R. Jr. (1999) BP and Oasis impact
690 structures, Libya, and their relation to Libyan Desert Glass. In B.O. Dressler and V.L.
691 Sharpton, Eds., Large Meteorite Impacts and Planetary Evolution, II, p. 177-192.
692 Geological Society of America Special Paper, 339, Boulder, Colorado.

693 Aboud, T. (2009) Libyan Desert Glass: has the enigma of its origin been resolved? Physics

694 Procedia, 2, 1425–1432.

695 Baker, G. (1959) Tektites. Memoirs of the National Museum of Victoria, 23, 313 p.
696 Melbourne, Australia.

697 Barakat, A.A., de Michele, V., Negro, G., Piacenza, B., and Serra, R. (1997) Some new data
698 on the distribution of Libyan Desert Glass (Great Sand Sea, Egypt). In V. de Michele,
699 Ed., Proceedings of the Meeting on Libyan Desert Glass and Related Desert Events
700 Silica'96, p. 29–36. Pyramids, Milan, Italy.

701 Barnes, V.E., and Underwood, J.R. Jr. (1976) New investigations of the strewn field of
702 Libyan Desert Glass and its petrography. Earth and Planetary Science Letters, 30,
703 117–122.

704 Barrat, J.A., Jahn, B.M., Amossé, J., Rocchia, R., Keller, F., Poupeau, G.R., and Diemer, E.
705 (1997) Geochemistry and origin of Libyan Desert glasses. Geochimica et
706 Cosmochimica Acta, 61, 1953–1959.

707 Beran, A., and Koeberl, C. (1997) Water in tektites and impact glasses by fourier-transformed
708 infrared spectrometry. Meteoritics & Planetary Science, 32, 211–216.

709 Bigazzi, G., and De Michele, V. (1996) New fission-track age determinations on impact
710 glasses. Meteoritics & Planetary Science, 31, 234–236.

711 Bigazzi, G., and De Michele, V. (1997) New fission-track ages of Libyan Desert Glass. In V.
712 de Michele, Ed., Proceedings of the Meeting on Libyan Desert Glass and Related
713 Desert Events Silica'96, p. 49–58. Pyramids, Milan, Italy.

714 Block, S., Da Jornada, J.A.H., and Piermarini, G.J. (1985) Pressure-temperature phase
715 diagram of zirconia. Journal of the American Ceramic Society, 68, 497–499.

716 Boehnke, P., Watson, E.B., Trail, D., Harrison, T.M., and Schmitt, A.K. (2013) Zircon
717 saturation re-revisited. Chemical Geology, 351, 324–334.

718 Borisov, A., and Aranovich, L. (2019) Zircon solubility in silicate melts: new experiments

719 and probability of zircon crystallization in deeply evolved basic melts. Chemical
720 Geology, 510, 103–112.
721 Boslough, M.B.E., and Crawford, D.A. (2008) Low altitude airbursts and the impact threat.
722 International Journal of Impact Engineering, 35, 1441–1448.
723 Boslough, M. (2014) Airburst warning and response. Acta Astronautica, 103, 370–375.
724 Bouvier, P., Djurado, E., Lucazeau, G., and Le Bihan, T. (2000) High-pressure structural
725 evolution of undoped tetragonal nanocrystalline zirconia. Physical Review B, 62,
726 8731–8737.
727 Boysen, H., Frey, F., and Vogt, T. (1991) Neutron powder investigation of the tetragonal to
728 monoclinic phase transformation in undoped zirconia. Acta Crystallographica, Section
729 B: Structural Science, 47, 881–886.
730 Brown, P.G., Assink, J.D., Astiz, L., Blaauw, R., Boslough, M.B., Borovička, J., Brachet, N.,
731 Brown, D., Campbell-Brown, M., Ceranna, L., Cooke, W., de Groot-Hedlin, C., Drob,
732 D.P., Edwards, W., Evers, L.G., Garces, M., Gill, J., Hedlin, M., Kingery, A., Laske,
733 G., Le Pichon, A., Mialle, P., Moser, D.E., Saffer, A., Silber, E., Smets, P., Spalding,
734 R.E., Spurný, P., Tagliaferri, E., Uren, D., Weryk, R.J., Whitaker, R., and Krzeminski,
735 Z. (2013) A 500-kiloton airburst over Chelyabinsk and an enhanced hazard from small
736 impactors. Nature, 503, 238–241.
737 Capitani, G.C., Leroux, H., Doukhan, J.C., Rios, S., Zhang, M., and Salje, E.K.H. (2000) A
738 TEM investigation of natural metamict zircons: structure and recovery of amorphous
739 domains. Physics and Chemistry of Minerals, 27, 545–556.
740 Cavosie, A.J., and Koeberl, C. (2019) Overestimation of threat from 100 Mt-class airbursts?
741 High-pressure evidence from zircon in Libyan Desert Glass. Geology, 47, 609–612.

742 Cavosie, A.J., Timms, N.E., Ferrière, L., and Rochette, P. (2018a) FRIGN zircon – The only
743 terrestrial mineral diagnostic of high-pressure and high-temperature shock
744 deformation. Geology, 46, 891–894.
745 Cavosie, A.J., Timms, N.E., Erickson, T.M., and Koeberl, C. (2018b) New clues from Earth's
746 most elusive impact crater: Evidence of reidite in Australasian tektites from Thailand.
747 Geology, 46, 203–206.
748 Cavosie, A.J., Rickard, W.D.A., Evans, N.J., Rankenburg, K., Roberts, M., Macris, C.A.,
749 Koeberl, C., (2022) Origin of β-cristobalite in Libyan Desert Glass: The hottest
750 naturally occurring silica polymorph? American Mineralogist, 107, 1325–1340.
751 Cayron, C., Douillard, T., Sibil, A., Fantozzi, G., and Sao-Jao, S. (2010) Reconstruction of the
752 cubic and tetragonal parent grains from electron backscatter diffraction maps of
753 monoclinic zirconia. Journal of the American Ceramic Society, 93, 2541–2544.
754 Chevalier, J., Gremillard, L., Virkar, A.V., and Clarke, D.R. (2009) The tetragonal-
755 monoclinic transformation in zirconia: Lessons learned and future trends. Journal of
756 the American Ceramic Society, 92, 1901–1920.
757 Clayton, P.A., and Spencer, L.J. (1934) Silica-glass from the Libyan Desert. Mineralogical
758 Magazine, 23, 501–508.
759 Cox, M., Erickson, T.M., Schmieder, M., Christoffersen, R., Ross, D.K., Cavosie, A.J., Bland,
760 P.A., Kring, D.A., and IODP–ICDP Expedition 364 Scientists (2020) High-resolution
761 microstructural and compositional analyses of shock deformed apatite from the peak
762 ring of the Chicxulub impact crater. Meteoritics & Planetary Science, 55, 1–19.
763 Darling, J.R., Moser, D.E., Barker, I.R., Tait, K.T., Chamberlain, K.R., Schmitt, A.K., Hyde,
764 B.C. (2016) Variable microstructural response of baddeleyite to shock metamorphism
765 in young basaltic shergottite NWA 5298 and improved U–Pb dating of Solar System
766 events. Earth and Planetary Science Letters, 444, 1–12.

767 Diemer, E. (1997) Libyan Desert Glass: An impactite. State of the art in July 1996. In V. de
768 Michele, Ed., Proceedings of the Meeting on Libyan Desert Glass and Related Desert
769 Events Silica'96, p. 95–110. Pyramids, Milan, Italy.
770 El Goresy, A. (1965) Baddeleyite and Its Significance in Impact Glasses. Journal of
771 Geophysical Research, 70, 3453–3456.
772 Erickson, T.M., Timms, N.E., Pearce, M.A., Cayron, C., Deutsch, A., Kelelr, L.P., and Kring,
773 D.A. (2019) Shock-produced high-pressure (La, Ce, Th)$PO_4$ polymorph revealed by
774 microstructural phase heritage of monazite. Geology, 47, 504–508.
775 Erickson, T.M., Kirkland, C.L., Timms, N.E., Cavosie, A.J., and Davison, T.M. (2020)
776 Precise radiometric age establishes Yarrabubba, Western Australia, as Earth's oldest
777 recognized meteorite impact structure. Nature Communication, 11, 300.
778 Feller, M. (1997) Vitreous silica from the Sahara. In V. de Michele, Ed., Proceedings of the
779 Meeting on Libyan Desert Glass and Related Desert Events Silica'96, p. 111–114.
780 Pyramids, Milan, Italy.
781 Frischat, G.H., Klöpfer, C., Beier, W., Weeks, R.A. (1984) Some properties of Libyan Desert
782 glasses. Journal of Non-Crystalline Solids, 67, 621–628.
783 Fröhlich, F., Poupeau, G., Badou, A., Le Bourdonnec, F.X., Sacquin, Y., Dubernet, S.,
784 Bardintzeff, J.M., Véran, M., Smith, D.C., and Diemer, E. (2013) Libyan Desert
785 Glass: New field and Fourier transform infrared data. Meteoritics & Planetary Science,
786 48, 2517–2530.
787 Fudali, R.F. (1981) The major element chemistry of Libyan Desert Glass and the mineralogy
788 of its precursor. Meteoritics, 16, 247–259.
789 Futrell, D.S., and O'Keefe, J.A. (1997) A brief discussion of the petrogenesis of Libyan
790 Desert Glass. In V. de Michele, Ed., Proceedings of the Meeting on Libyan Desert
791 Glass and Related Desert Events Silica'96, p. 115–120. Pyramids, Milan, Italy.

792 Gentner, W., Storzer, D., and Wagner, G.A. (1969) New fission track ages of tektites and
793 related glasses. Geochimica et Cosmochimica Acta, 33, 1075–1081.
794 Gervasoni, F., Klemme, S., Rocha-Júnior, E.R.V., and Berndt, J. (2016) Zircon saturation in
795 silicate melts: a new and improved model for aluminous and alkaline melts.
796 Contributions to Mineralogy and Petrology, 171, 21.
797 Giuli, G., Paris, E., Pratesi, G., Koeberl, C., and Cipriani, C. (2003) Iron oxidation state in Fe-
798 rich layer and silica matrix of Libyan Desert Glass: A high-resolution XANES study.
799 Meteoritics & Planetary Science, 38, 1181–1186.
800 Gleiter, H. (1989) Nanocrystalline Materials. Progress in Materials Science, 33, 223–315.
801 Greshake, A., Koeberl, C., Fritz, J., and Reimold, W.U. (2010) Brownish inclusions and dark
802 streaks in Libyan Desert Glass: Evidence for high-temperature melting of the target
803 rock. Meteoritics & Planetary Science, 45, 973–989.
804 Greshake, A., Wirth, R., Fritz, J., Jakubowski, T., and Böttger, U. (2018) Mullite in Libyan
805 Desert Glass: Evidence for high-temperature/low pressure formation. Meteoritics &
806 Planetary Science, 53, 467–481.
807 Gu, L., Wang, N., Tang, X., and Changela, H.G. (2020) Application of FIB-SEM Techniques
808 for the Advanced Characterization of Earth and Planetary Materials. Scanning, 2020,
809 8406917.
810 Haines, J., Leger, J.M., and Atouf, A. (1995) Crystal structure and equation of state of
811 cotunnite-type zirconia. Journal of the American Ceramic Society, 78, 445–448.
812 Haines, J., Leger, J.M., Hull, S., Petitet, J.P., Pereira, A.S., Perottoni, C.A., and da Jornada,
813 J.A.H. (1997) Characterization of the cotunnite-type phases of zirconia and hafnia by
814 neutron diffraction and Raman spectroscopy. Journal of the American Ceramic
815 Society, 80, 1910–1914.

816 Harrison, T.M., Watson, E.B., and Aikman, A.B. (2007) Temperature spectra of zircon
817 crystallization in plutonic rocks. Geology, 35, 635–638.
818 Hauser, N., Reimold, W.U., Cavosie, A.J., Crósta, A.P., Schwarz, W.H., Trieloff, M., Da
819 Silva Maia de Souza, C., Pereira, L.A., Rodrigues, E.N., and Brown, M. (2019)
820 Linking shock textures revealed by BSE, CL, and EBSD with U-Pb data (LA-ICPMS
821 and SIMS) from zircon from the Araguainha impact structure, Brazil. Meteoritics &
822 Planetary Science, 54, 2286–2311.
823 Hikichi, Y., and Nomura, T. (2005) Melting temperature of monazite and xenotime. Journal
824 of the American Ceramic Society, 70, C-252–C-253.
825 Horn, P., Müller-Sohnius, D., Schaaf, P., Kleinmann, B., and Storzer, D. (1997) Potassium-
826 argon and fission-track dating of Libyan Desert Glass, and strontium and neodymium
827 isotope constraints in its source rocks. In V. de Michele, Ed., Proceedings of the
828 Meeting on Libyan Desert Glass and Related Desert Events Silica'96, p. 59–76.
829 Pyramids, Milan, Italy.
830 Jimenez-Martinez, N., Ramirez, M., Diaz-Hernandez, R., and Rodriguez-Gomez, G. (2015)
831 Fluvial transport model from spatial distribution analysis of Libyan Desert Glass mass
832 on the Great Sand Sea (Southwest Egypt): clues to primary glass distribution.
833 Geosciences, 5, 95–116.
834 Jux, U. (1983) Zusammensetzung und Ursprung von Wüstengläsern aus der Großen Sandsee
835 Ägyptens. Zeitschrift der Deutschen Geologischen Gesellschaft, 134, 521–553.
836 Kaiser, A., Lobert, M., and Telle, R. (2008) Thermal stability of zircon ($ZrSiO_4$). Journal of
837 the European Ceramic Society, 28, 2199–2211.
838 Kaneko, S., Miyahara, M., Ohtani, E., Arai, T., Hirao, N., and Sato, K. (2015) Discovery of
839 stishovite in Apollo 15299 sample. American Mineralogist, 100, 1308–1311.

840 Keller, L.P., Berger, E.L., Zhang, S., and Christoffersen, R. (2021) Solar energetic particle
841 tracks in lunar samples: A transmission electron microscope calibration and
842 implications for lunar space weathering. Meteoritics & Planetary Science, 56, 1685–
843 1707.
844 Kenny, G.G., and Pasek, M.A. (2021) The response of zircon to the extreme pressures and
845 temperatures of a lightning strike. Scientific Reports, 11, 1560.
846 Kenny, G.G., Morales, L.F., Whitehouse, M.J., Petrus, J.A., and Kamber, B.S. (2017) The
847 formation of large neoblasts in shocked zircon and their utility in dating impacts.
848 Geology, 45, 1003–1006.
849 Kenny, G.G., Schmieder, M., Whitehouse, M.J., Nemchin, A.A., Morales, L.F.G., Buchner,
850 E., Bellucci, J.J., and Snape, J.F. (2019) A new U-Pb age for shock-recrystallised
851 zircon from the Lappajärvi impact crater, Finland, and implications for the accurate
852 dating of impact events. Geochimica et Cosmochimica Acta, 245, 479–494.
853 Kenny, G.G., Karlsson, A., Schmieder, M., Whitehouse, M.J., Nemchin, A.A., and Bellucci,
854 J.J. (2020) Recrystallization and chemical changes in apatite in response to
855 hypervelocity impact. Geology, 48, 19–23.
856 Khisina, N.R., Wirth, R., Nazarov, M.A., (2011) Lamellar Pyroxene–Spinel Symplectites in
857 Lunar Olivine from the Luna 24 Regolith. Geochemistry International, 49, 449–458.
858 Kleinmann, B. (1968) The breakdown of zircon observed in the Libyan Desert Glass as
859 evidence of its impact origin. Earth and Planetary Science Letters, 5, 497–501.
860 Kleinmann, B., Horn, P., and Langenhorst, F. (2001) Evidence for shock metamorphism in
861 sand stones from the Libyan Desert Glass strewn field. Meteoritics & Planetary
862 Science, 36, 1277–1282.

863 Koeberl, C. (1997) Libyan Desert Glass: Geochemical composition and origin. In V. de
864 Michele, Ed., Proceedings of the Meeting on Libyan Desert Glass and Related Desert
865 Events Silica'96, p. 121 – 131. Pyramids, Milan, Italy.
866 Koeberl, C. (2000) Confirmation of a meteoritic component in Libyan Desert Glass from
867 osmium-isotopic data. Meteoritics & Planetary Science, 35, A89–A90.
868 Koeberl, C., and Ferriere, L. (2019) Libyan Desert Glass area in western Egypt: shocked
869 quartz in bedrock points to a possible deeply eroded impact structure in the region.
870 Meteoritics & Planetary Science 54, 2398–2408.
871 Kovaleva, E., Kusiak, M.A., Kenny, G.G., Whitehouse, M.J., Schreiber, A., and Wirth, R.
872 (2021) Nano-scale investigation of granular neoblastic zircon, Vredefort impact
873 structure, South Africa: Evidence for complete shock melting. Earth and Planetary
874 Science Letters, 565, 116948.
875 Kusiak, M.A., Wilde, S.A., Wirth, R., Whitehouse, M.J., Dunkley, D.J., Lyon, I., Reddy,
876 S.M., Berry, A., and de Jonge, M. (2018) Detecting Micro- and Nanoscale Variations
877 in Element Mobility in High-Grade Metamorphic Rocks: Implication for Precise U-Pb
878 Dating of Zircon. In D.E. Moser, F. Corfu, J.R. Darling, S.M. Reddy and K. Tait, Eds.,
879 Microstructural Geochronology: Planetary Records Down to Atom Scale, p. 279–291.
880 American Geophysical Union Geophysical Monographs, 232.
881 Kwon, S.Y., and Jung, I. (2017) Critical evaluation and thermodynamic optimization of the
882 $CaO$-$ZrO_2$ and $SiO_2$-$ZrO_2$ systems. Journal of the European Ceramic Society, 37,
883 1105–1116.
884 Leroux, H., and Cordier, P. (2006) Magmatic cristobalite and quartz in the NWA 856 Martian
885 meteorite. Meteoritics & Planetary Science, 41, 913–923.

886 Leroux, H., Reimold, W.U., Koeberl, C., Hornemann, U., and Doukhan, J.-C. (1999)
887 Experimental shock deformation in zircon: A transmission electron microscopic study.
888 Earth and Planetary Science Letters, 169, 291–301.
889 Liu, L.-G. (1980) New high pressure phases of $ZrO_2$ and $HfO_2$. Journal of Physics and
890 Chemistry of Solids, 41, 331–334.
891 Martin, U., Boysen, H., and Frey, F. (1993) Neutron powder investigation of tetragonal and
892 cubic stabilized zirconia, TZP and CSZ, at temperatures up to 1400K. Acta
893 Crystallographica, Section B: Structural Science, 49, 403–413.
894 McCubbin, F.M., Barnes, J.J., Srinivasan, P., Whitson, E.S., Vander Kaaden, K.E., and Boyce,
895 J.W. (2017) Experimental study into the stability of whitlockite in basaltic magmas.
896 Proceedings of the 80th Annual Meeting of the Meteoritical Society, Lunar and
897 Planetary Iinstitute Contribution No 1987.
898 McCullough, J.D., Trueblood, K.N. (1959) The crystal structure of baddeleyite (monoclinic
899 $ZrO_2$). Acta Crystallographica, 12, 507–511.
900 Melosh, H.J. (2007) A hydrocode equation of state for $SiO_2$. Meteoritics & Planetary Science,
901 42, 2079–2098.
902 Murali, A.V., Zolensky, M.E., Underwood, J.R. Jr., and Giegengack, R.F. (1997) Chondritic
903 debris in Libyan Desert Glass. In V. de Michele, Ed., Proceedings of the Meeting on
904 Libyan Desert Glass and Related Desert Events Silica'96, p. 133–142. Pyramids,
905 Milan, Italy.
906 Nassau, K. (1981) Cubic zirconia: an update. Gems & Gemology, 17, 9–19.
907 Ohtaka, O., Yamanaka, T., Kume, S., Ito, E., and Navrotsky, A. (1991) Stability of
908 monoclinic and orthorhombic zirconia: Studies by high-pressure phase equilibria and
909 calorimetry. Journal of the American Ceramic Society, 74, 505–509.

Ohtaka, O., Fukui, H., Kunisada, T., Fujisawa, T., Funakoshi, K., Utsumi, W., Irifune, T., Kuroda, K., and Kikegawa, T. (2001) Phase relations and equations of state of $ZrO_2$ under high temperature and high pressure. Physical Review B, 63, 174108.

Rodionov, N.V., Belyatsky, B.V., Antonov, A.V., Kapitonov, I.N., Sergeev, S.A.,Pratesi, G., Viti, C., Cipriani, C., and Mellini, M. (2002) Silicate–silicate liquid immiscibility and graphite ribbons in Libyan Desert Glass. Geochimica et Cosmochimica Acta, 66, 903–911.

Reimold, W.U., Leroux, H., and Gibson, R.L. (2002) Shocked and thermally metamorphosed zircon from the Vredefort impact structure, South Africa: a transmission electron microscopic study. European Journal of Mineralogy, 14, 859–868.

Rocchia, R., Robin, E., Fröhlich, F., Méon, H., Froget, L., and Diemer, E. (1996) L'origine des verres du désert libyque: un impact météoritique. Comptes rendus de l'Académie des Sciences, 322 (Ser. IIa), 839–845.

Schnurre, S.M., Gröbner, J., and Schmid-Fetzer, R. (2004) Thermodynamics and phase stability in the Si–O system. Journal of Non-Crystalline Solids, 366, 1–25.

Seebaugh, R., and Strauss, M. (1984) A cometary impact model for the source of Libyan Desert Glass. Journal of Non-Crystalline Solids, 67, 511–519.

Seydoux-Guillaume, A.-M., Bingen, B., Bosse, V., Janots, E., and Laurent, A.T. (2018) Transmission Electron Microscope Imaging Sharpens Geochronological Interpretation of Zircon and Monazite. In D.E. Moser, F. Corfu, J.R. Darling, S.M. Reddy and K. Tait, Eds., Microstructural Geochronology: Planetary Records Down to Atom Scale, p. 261–275. American Geophysical Union Geophysical Monographs, 232.

Shao, T., Xia, Y., Ding, X., Cai, Y., and Song, M. (2020) Zircon saturation model in silicate melts: a review and update. Acta Geochimica, 39, 387–403.

Subbarao, E.C. (1981) Zirconia – an overview. In A.H. Heuer and L.W. Hobbs, Eds., Advances in Ceramics, p. 1–24. American Ceramic Society.

Suyama, R., Ashida, T., and Kume, S. (1985) Synthesis of orthorhombic phase of $ZrO_2$. Journal of the American Ceramic Society, 68, C314–C315.

Svetsov, V.V., and Watson, J.T. (2007) Melting of soil rich in quartz by radiation from aerial bursts – A possible cause of formation of Libyan Desert Glass and layered tektites. In Proceedings of the Lunar and Planetary Science conference XXXVIII, 1499. Lunar and Planetary Institute, Houston.

Timms, N.E., Erickson, T.M., Pearce, M.A., Cavosie, A.J., Scmieder, M., Tohver, E., Reddy, S.M., Zanetti, M.R., Nemchin, A.A., and Wittmann, A. (2017) A pressure-temperature phase diagram for zircon at extreme conditions. Earth-Science Reviews, 165, 185–202.

Tolometti, G.D., Erickson, T.M., Osinski, G.R., Cayron, C., Neish, C.D. (2022) Hot rocks: Constraining the thermal conditions of the Mistastin Lake impact melt deposits using zircon grain microstructures. Earth and Planetary Science Letters, 584, 117523.

Urey, H.C. (1957) Origin of tektites. Nature, 179, 556–557.

Wasson, J.T. (2003) Large aerial bursts: An important class of terrestrial accretionary events. Astrobiology, 3, 163–179.

Watson, E.B., and Harrison, T.M. (1983) Zircon saturation revisited: temperature and composition effects in a variety of crustal magma types. Earth and Planetary Science Letters, 64, 295–304.

Weeks, R.A., Underwood, J.R. Jr., and Giegengack, R. (1984) Libyan Desert glass: A review. Journal of Non-Crystalline Solids, 67, 593–619.

Wentworth, S.J., Keller, L.P., McKay, D.S., Morris, R.V. (1999) Space weathering on the Moon: Patina on Apollo 17 samples 75075 and 76015. Meteoritics & Planetary Science, 34, 593–603.

White, L.F., Darling, J.R., Moser, D.E., Cayron, C., Barker, I., Dunlop, J., and Tait, K.T. (2018) Baddeleyite as a widespread and sensitive indicator of meteorite bombardment in planetary crusts. Geology, 46, 719–722.

Wittmann, A., Kenkmann, T., Schmitt, R.T., and Stöffler, D. (2006) Shock-metamorphosed zircon in terrestrial impact craters. Meteoritics & Planetary Science, 41, 433–454.

Wittmann, A., Schmitt, R.T., Hecht, L., Kring, D.A., Reimold, W.U., and Povenmire, H. (2009) Petrology of impact melt rocks from the Chesapeake Bay crater, USA. In G.S. Gohn, C. Koeberl, K.G. Miller and W.U. Reimold, Eds., The ICDP-USGS Deep Drilling Project in the Chesapeake Bay Impact Structure: Results from the Eyreville Core Holes, p. 377–396. Geological Society of America Special Paper, 458, Boulder, Colorado.

Jin, X.-J. (2005) Martensitic transformation in zirconia containing ceramics and its applications. Current Opinion in Solid State & Materials Science, 9, 313–318.

**Figure captions**

**Figure 1**. Sampling location and samples. (**a**) Northern Africa with the area of interest shown by the red rectangle. Inset shows larger context of the sampling area. (**b**) Area of sample collection showing a vertical border between Libya and Egypt in the center. Two sites labeled "BP" and "Oasis" in southeast of Libya are the nearest described impact structures (e.g., Abate et al., 1999). LDG strewn field is marked by an ellipse in west of Egypt. Maps are created from Qgis. (**c**) Photographs of two studied samples that represent small (2-3 cm) angular fragments of yellow transparent to translucent glass. Air vesicles are visible inside.

**Figure 2.** BSE images of $ZrO_2$ (**a**) and zircon (**b**) granular aggregates (bright) enclosed within the $SiO_2$ glass (dark). Both aggregates appear to be stretched and pulled apart. Aggregate in (a) was studied in a FIB foil A#6408, aggregate in (b) was studied in a FIB foil A#6409.

**Figure 3.** Examples of three textural groups of Zr-bearing mineral aggregates in TEM foils (all images are HAADF). (**a**) Group 1 – isolated elliptical granules of $ZrO_2$ (bright) surrounded by $SiO_2$ glass (dark). No zircon phase is observed. Foil B#6379. (**b**) Group 2 – texture comprises two domains: granular zircon with densely packed granules (top) and $ZrO_2$-$SiO_2$ emulsion with disconnected $ZrO_2$ grains (bottom). The transition between two domains is gradual. Foil B#6371. (**c**) Group 3 – granular aggregate of zircon. Inclusions of $ZrO_2$ and $SiO_2$ are visible as bright and dark particles accordingly inside the zircon granular mass. Foil A#6377. Presumably, all three textural group developed after single grains of zircon.

**Figure 4.** Details of textural group 1 (isolated granules of $ZrO_2$ in $SiO_2$ glass), FIB foil B#6410. (**a**) BSE image of the studied aggregate, white line shows the position of the TEM foil. (**b**) TEM FIB foil overview. Isolated elliptical, dumbbell-shaped or spherical grains of $ZrO_2$ (bright) are enclosed into $SiO_2$ glass (dark). Larger $ZrO_2$ grains are baddeleyite, indicated by their twinned texture. The HAADF image. Boxes mark the positions of images (c) and (d). (**c**) BF and (**d**) HAADF images of spherical inclusions of cubic zirconia (round) close up, with their FFT diffraction patterns in the insets. FFT patterns point at cubic symmetry of these crystals. The grain in (c) has a [001] zone axis, and the one in (d) has a [-101] zone axis orientation.

**Figure 5.** Details of textural group 2, foil A#6376. (**a**) BSE image of the studied aggregate, isolated grains of baddeleyite are at the left, and packed granular zircon is at the right. White line shows the position of the TEM foil. (**b**) TEM FIB foil overview. Baddeleyite crystals are the brightest, zircon grains are intermediate-grey and $SiO_2$ glass is the darkest in this HAADF image. (**c**) EDX spectrum of host $SiO_2$ glass (obtained with TEM). Minor peaks of P and Al

are observed, Cu peaks are from the copper grid that is holding the FIB foil. (**d**) Close-up image of the transition zone. The grey contrast represents zircon, the dark contrast stands for amorphous $SiO_2$, and the bright contrast shows baddeleyite. Some baddeleyite grains have zircon rims, zircon mass in the upper right has small inclusions of baddeleyite and $SiO_2$ glass. HAADF Z-contrast image.

**Figure 6.** More details on aggregate shown in Figure 5, foil A#6376. (**a**) Granular zircon domain up-close. Triple junctions are visible between the granules (circles). Zr-oxide spherical inclusions in zircon appear as dark contrast spots because of the higher absorption of electrons (black arrows). The amorphous $SiO_2$ inclusions have a brighter contrast than the zircon matrix because of lower electron absorption (white arrows). BF image. (**b**) High-resolution image of the representative example of tetragonal $ZrO_2$ inclusion that is approximately 18 nm in diameter and has a rectangular shape (BF image). Lattice fringes are visible (subvertical rows). The FFT diffraction pattern is shown in the inset, demonstrating tetragonal symmetry of the crystal. Additional diffraction spots in the diffraction pattern result from the zircon matrix. (**c**) A detailed view of the round baddeleyite grains (dark) rimmed with the nm-thick zircon layer (intermediate-grey, arrow) surrounded by $SiO_2$ glass (light-grey). BF image. (**d**) FFT diffraction patterns of different domains visible in (c): zircon rims (top) that are observed around baddeleyite cores (bottom). Numbers indicate the orientation of crystallographic planes.

**Figure 7.** Details of textural group 3, foil B#6411. (**a**) BSE image of the studied grain hosted by $SiO_2$ glass. Sub-μm inclusions visible inside zircon are $SiO_2$ glass (dark) $ZrO_2$ (bright). White line shows the position of the TEM foil. (**b**) TEM FIB foil overview displays the vertical extension of the originally idiomorphic zircon grain (now granular aggregate). Granules are densely packed, dark and bright inclusions are $SiO_2$ glass and $ZrO_2$ accordingly. The HAADF image. Bright vermicular and round inclusions are visible in matrix around the

aggregate. Box shows the position of image (c), with the details of the matrix. (**c**) Close-up portion of the glassy matrix, BF image. Vermicular grains are zircon, dark spherical inclusion is cubic zirconia with its FFT diffraction pattern shown in the inset.

**Figure 8.** More details on textural group 3. (**a**) BF image showing a typical densely-packed microstructure of the main mass of the granular neoblastic zircon. Triple junctions between granules are ubiquitous, and black arrows point at dark nano-inclusions of $ZrO_2$. (**b**) Granular zircon at the interface with the $SiO_2$ glass with inclusions of orthorhombic $ZrO_2$. Foil A#6409, BF image. The diffraction pattern of the orthorhombic $ZrO_2$ is shown in the inset. (**c**) High-resolution image of cubic zirconia inclusion with visible lattice fringes, BF image. The FFT diffraction pattern in on the right.

**Figure 9.** (**a**) BSE image of the elliptical whitlockite grain, white line shows the position of the TEM foil A#6378. (**b**) HAADF Z-contrast image showing the FIB foil overview of a corresponding cross-section through this inclusion. Main whitlockite grain is mosaic, i.e., is composed of subgrains, and has multiple dark nm-size pores. Smaller spherical inclusions of whitlockite are distributed in the host glass matrix. (**c**) EDX spectrum of the whitlockite (obtained with TEM), showing its chemical composition. (**d**) FFT diffraction pattern of whitlockite.

**Figure 10.** (**a**) TEM FIB foil overview of the mosaic whitlockite grain with spherical amorphous inclusions with berlinite composition. Foil A #6366, HAADF image Z-contrast image. (**b**) Close-up view of interior of whitlockite with amorphous inclusions with berlinite composition (dark) and subgrain boundaries (bright lines), HAADF image Z-contrast image. (**c**) EDX spectrum compositionally corresponding to berlinite – Al-phosphate (obtained with TEM). (**d**) FFT diffraction patterns of whitlockite (crystalline, sharp diffraction points) and amorphous berlinite (no diffraction points).

**Figure 11.** (**a**) BSE image of mosaic monazite (bright) with $SiO_2$ inclusions (dark), enclosed in $SiO_2$ glass matrix. Black line shows the position of the FIB foil B#6499. (**b**) The HAADF image displaying the FIB foil cut normal to the SEM surface demonstrates that the monazite inclusion is nearly spherical and contains spherical inclusions of $SiO_2$ (dark). (**c**) Close-up image showing the $SiO_2$ inclusions and low-angle boundaries inside the monazite, BF image. (**d**) FFT diffraction pattern of monazite with indexed planes. (**e**) EDX spectra of monazite, obtained with TEM, showing its chemical composition.

**Figure 12.** BF image of intensely twinned cristobalite with its FFT diffraction pattern in the inset in lower right.

# Figure 1

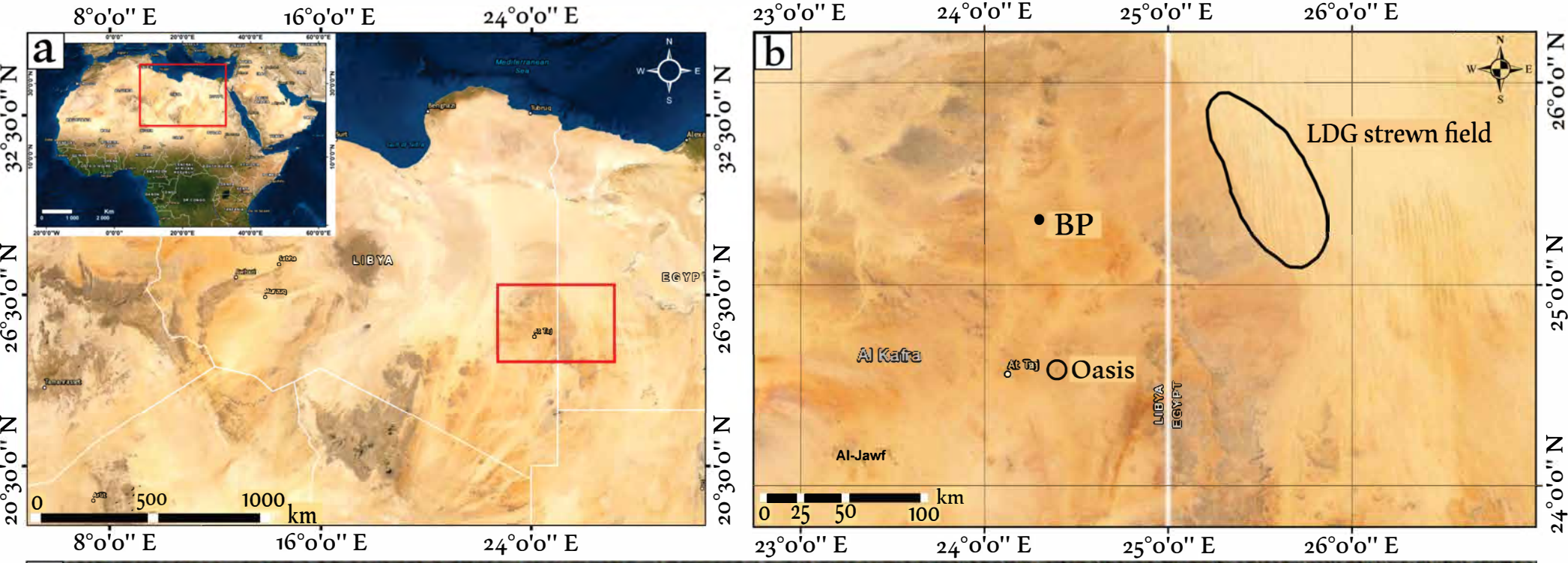
a
8°0'0" E
16°0'0" E
24°0'0" E
32°30'0" N
26°30'0" N
20°30'0" N
LIBYA
EGYP
0
500
1000
km
b
23°0'0" E
24°0'0" E
25°0'0" E
26°0'0" N
25°0'0" N
24°0'0" N
LDG strewn field
BP
Al Kafra
Oasis
Al-Jawf
LIBYA
EGYPT
0
25
50
100
km

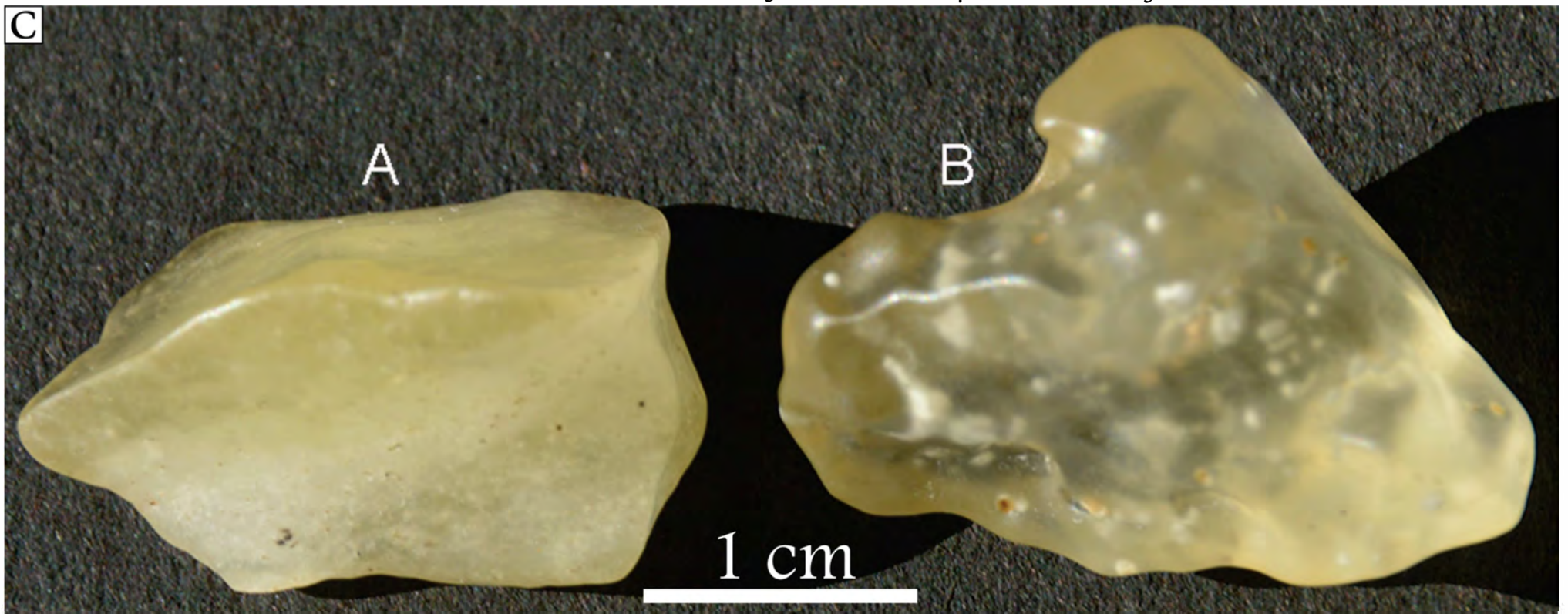
C
A
B
1 cm

# Figure 2

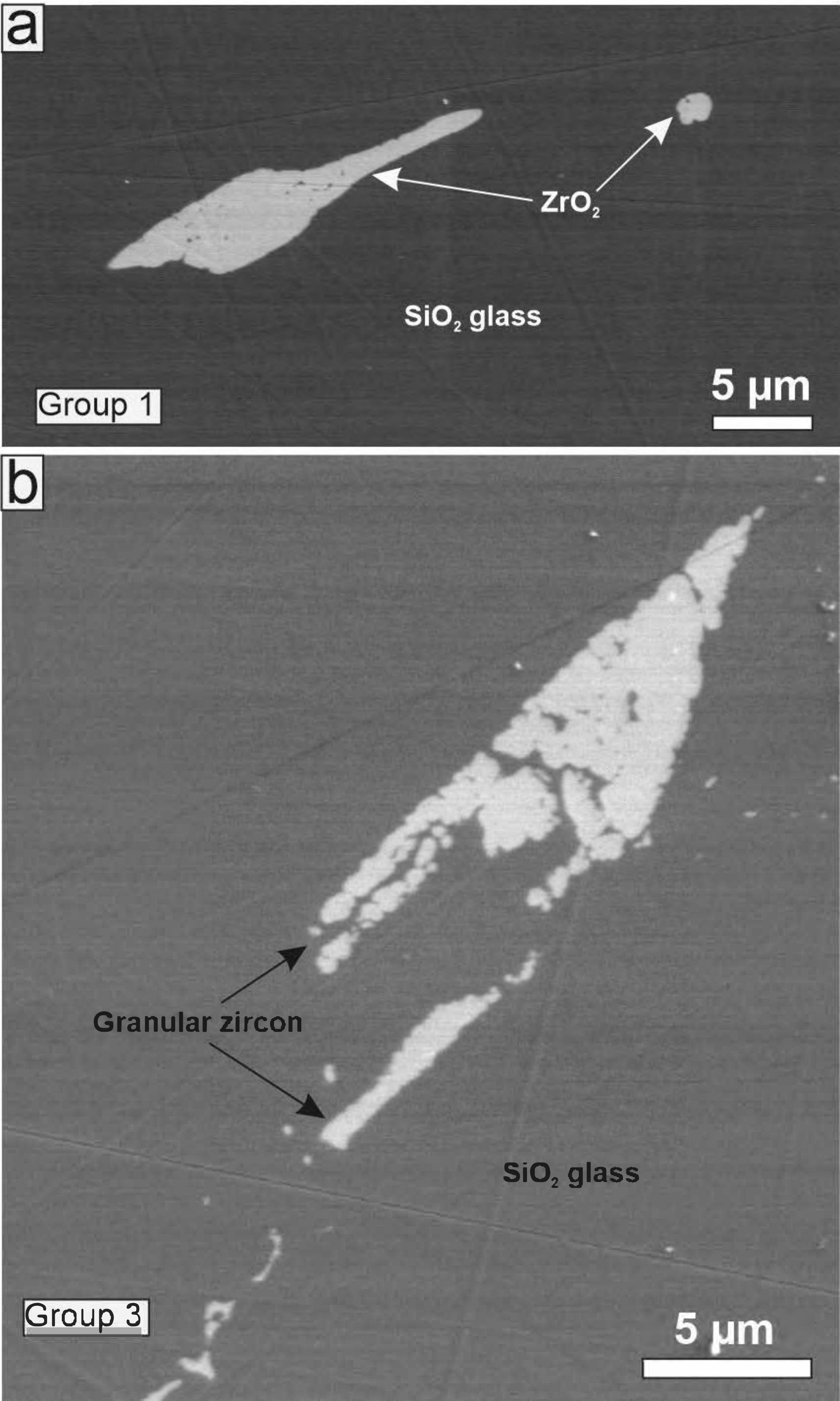
a
$ZrO_2$
$SiO_2$ glass
Group 1
5 µm
b
Granular zircon
$SiO_2$ glass
Group 3
5 µm

# Figure 3

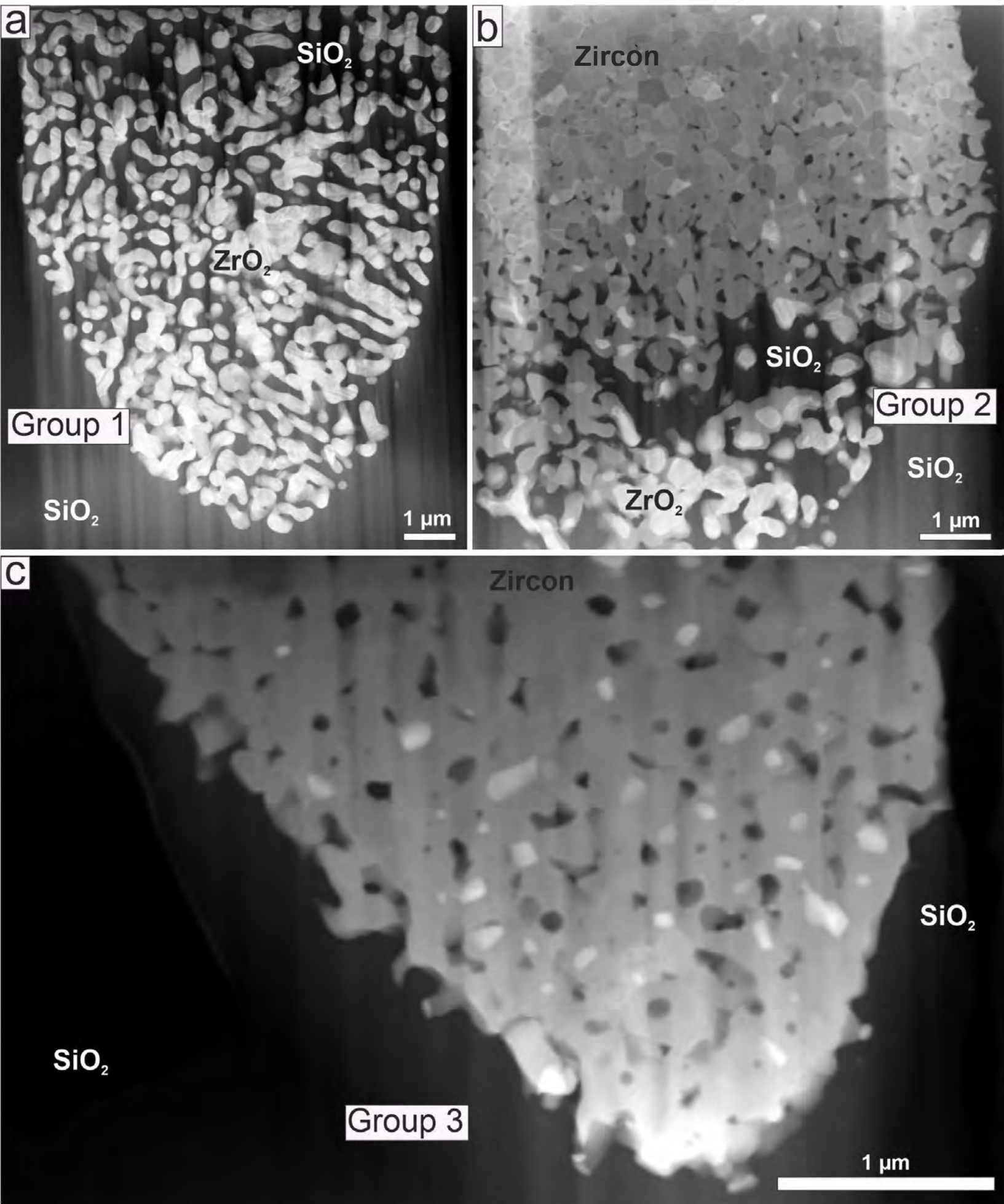
a
SiO2
ZrO2
Group 1
SiO2
1 µm
b
Zircon
SiO2
Group 2
SiO2
ZrO2
1 µm
c
Zircon
SiO2
SiO2
Group 3
1 µm

Figure 4

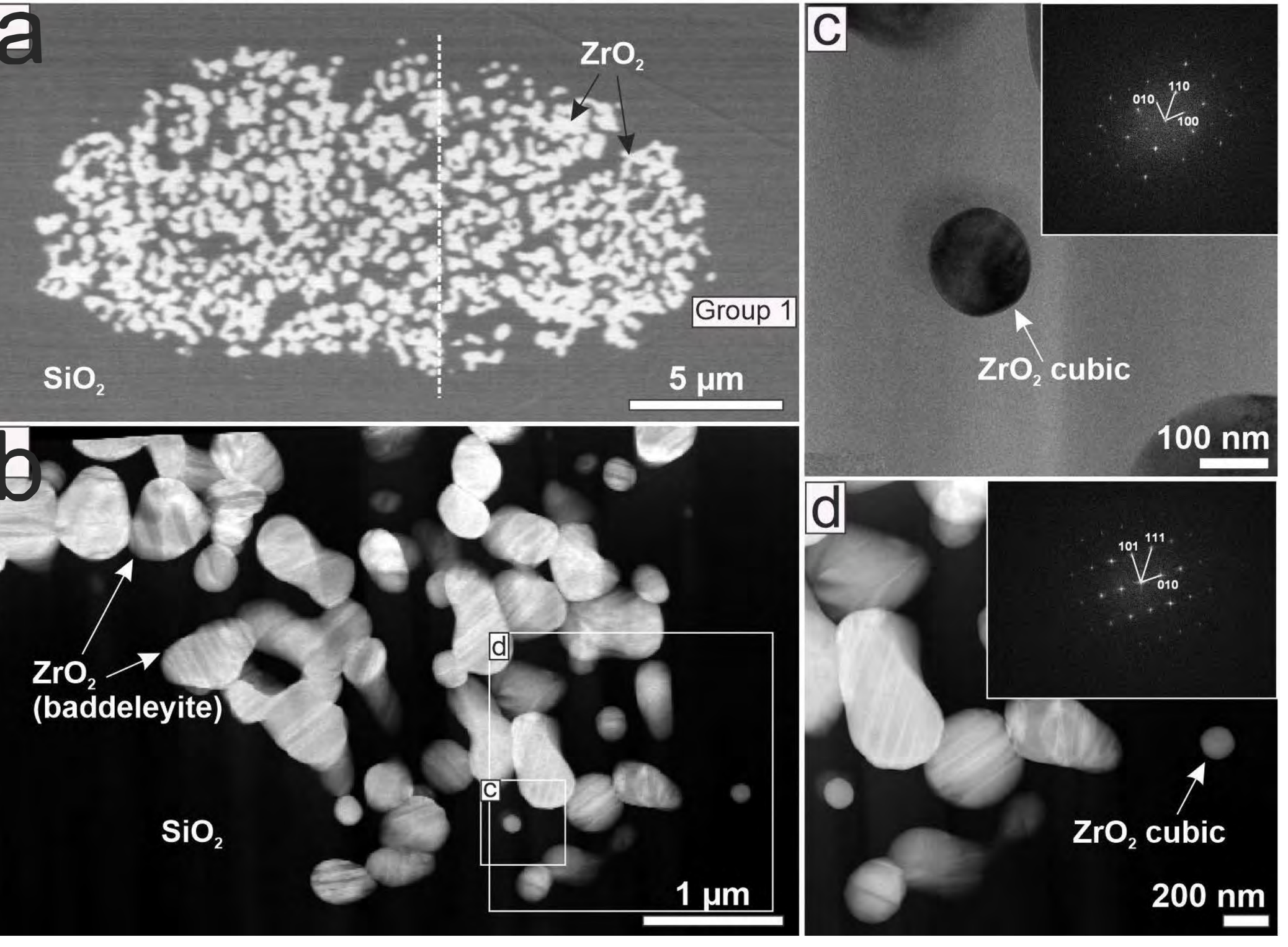
a
$ZrO_2$
Group 1
$SiO_2$
5 µm
b
$ZrO_2$
(baddeleyite)
d
c
$SiO_2$
1 µm
c
110
010
100
$ZrO_2$ cubic
100 nm
d
101
111
010
$ZrO_2$ cubic
200 nm

# Figure 5

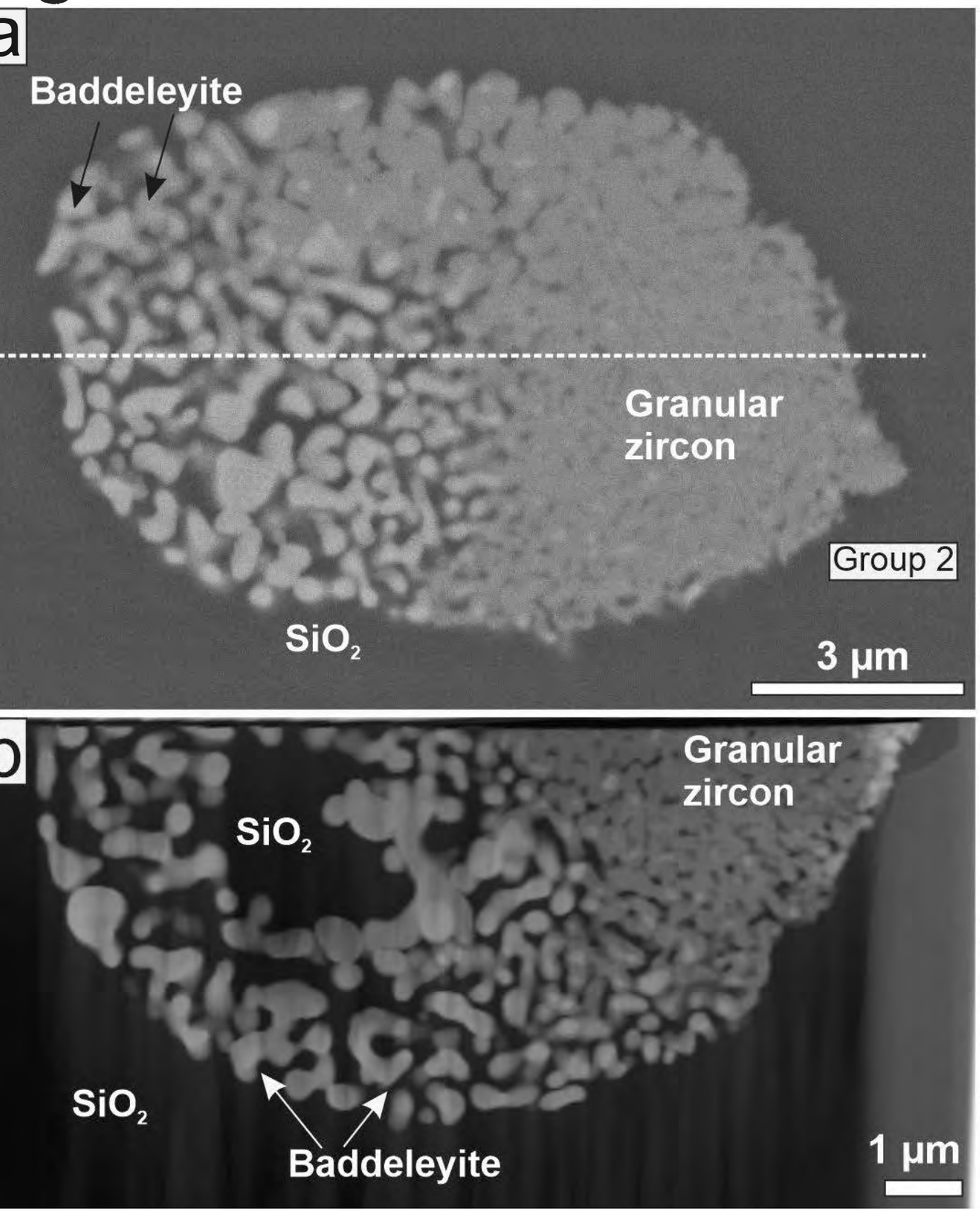
a
Baddeleyite
Granular zircon
Group 2
SiO2
3 µm
b
Granular zircon
SiO2
SiO2
Baddeleyite
1 µm

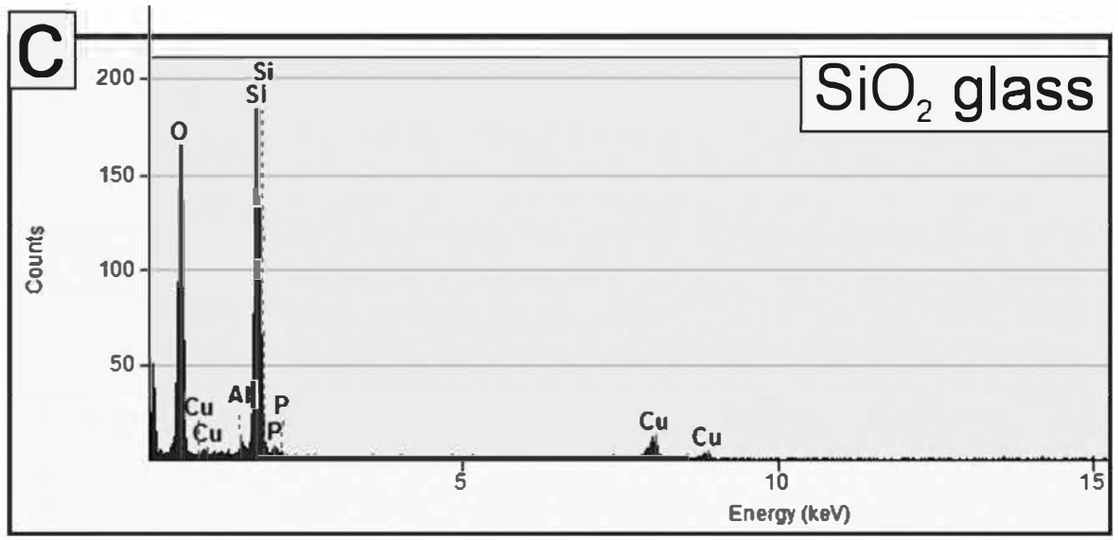
c
SiO2 glass
Counts
200
150
100
50
O
Si
Si
Cu
Cu
Al
P
P
Cu
Cu
5
10
15
Energy (keV)

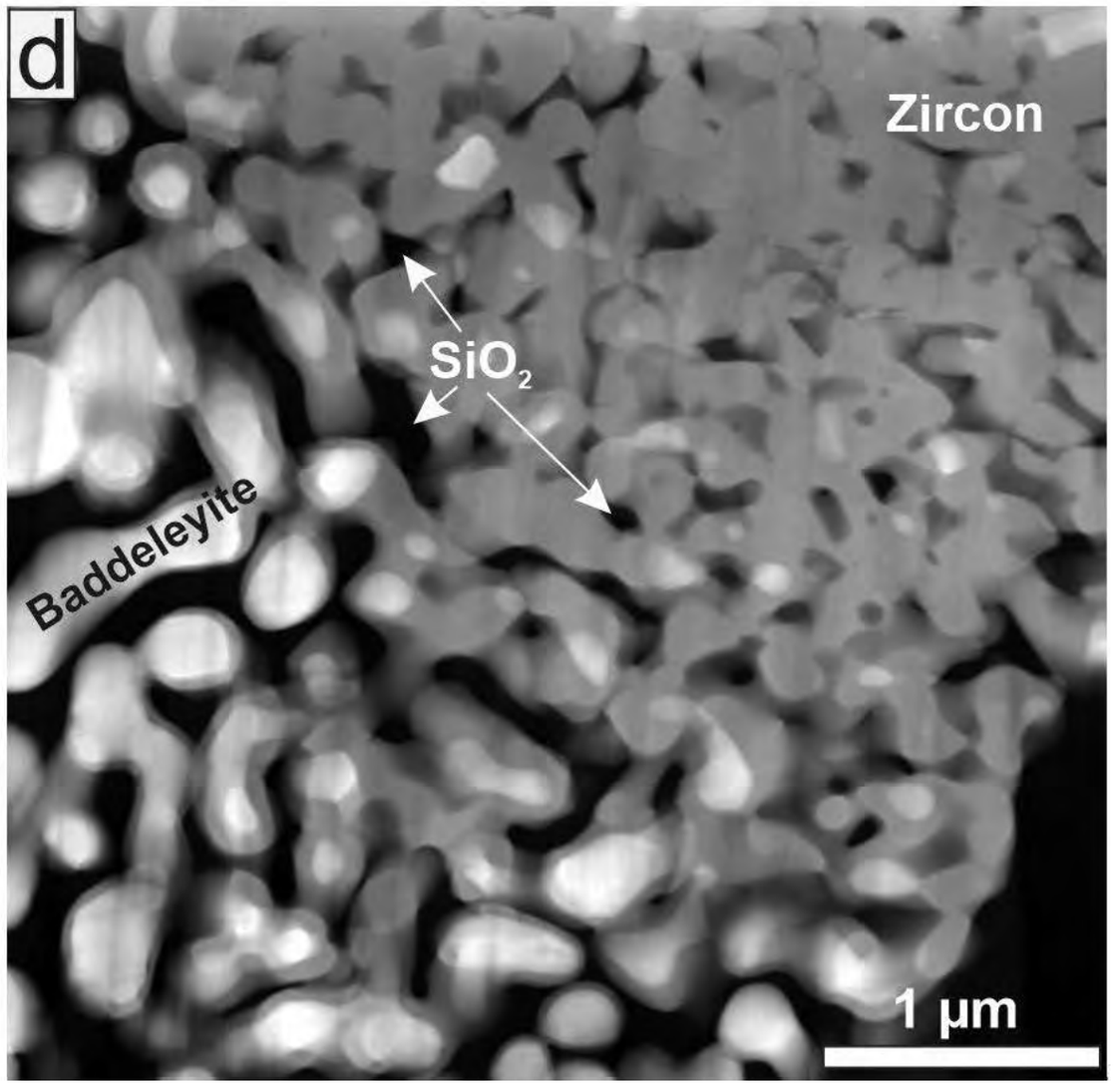
d
Zircon
SiO2
Baddeleyite
1 µm

# Figure 6

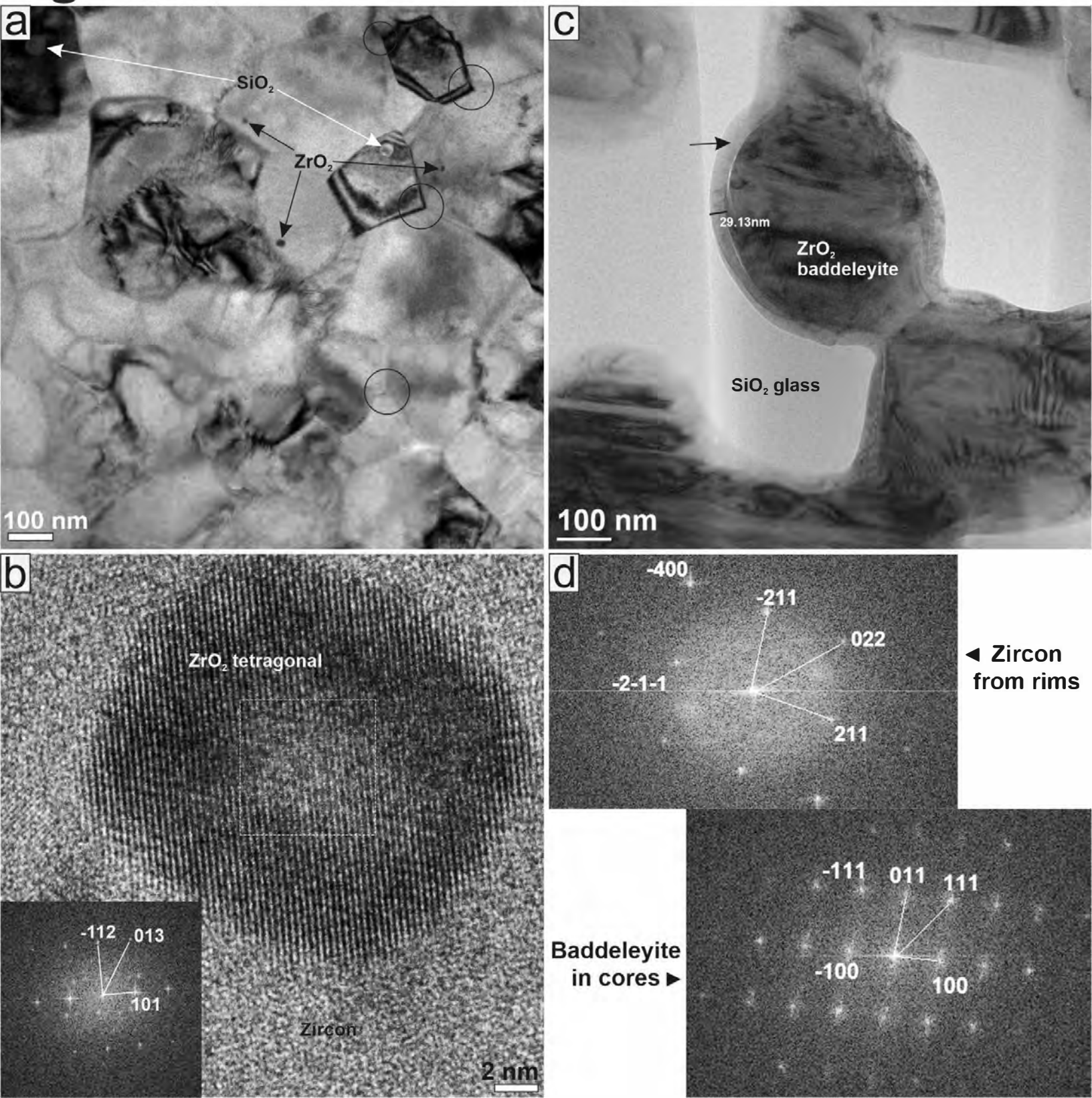
a
SiO2
ZrO2
100 nm
c
29.13nm
ZrO2
baddeleyite
SiO2 glass
100 nm
b
ZrO2 tetragonal
-112
013
101
Zircon
2 nm
d
-400
-211
022
-2-1-1
211
◄ Zircon
from rims
Baddeleyite
in cores ►
-111
011
111
-100
100

# Figure 7

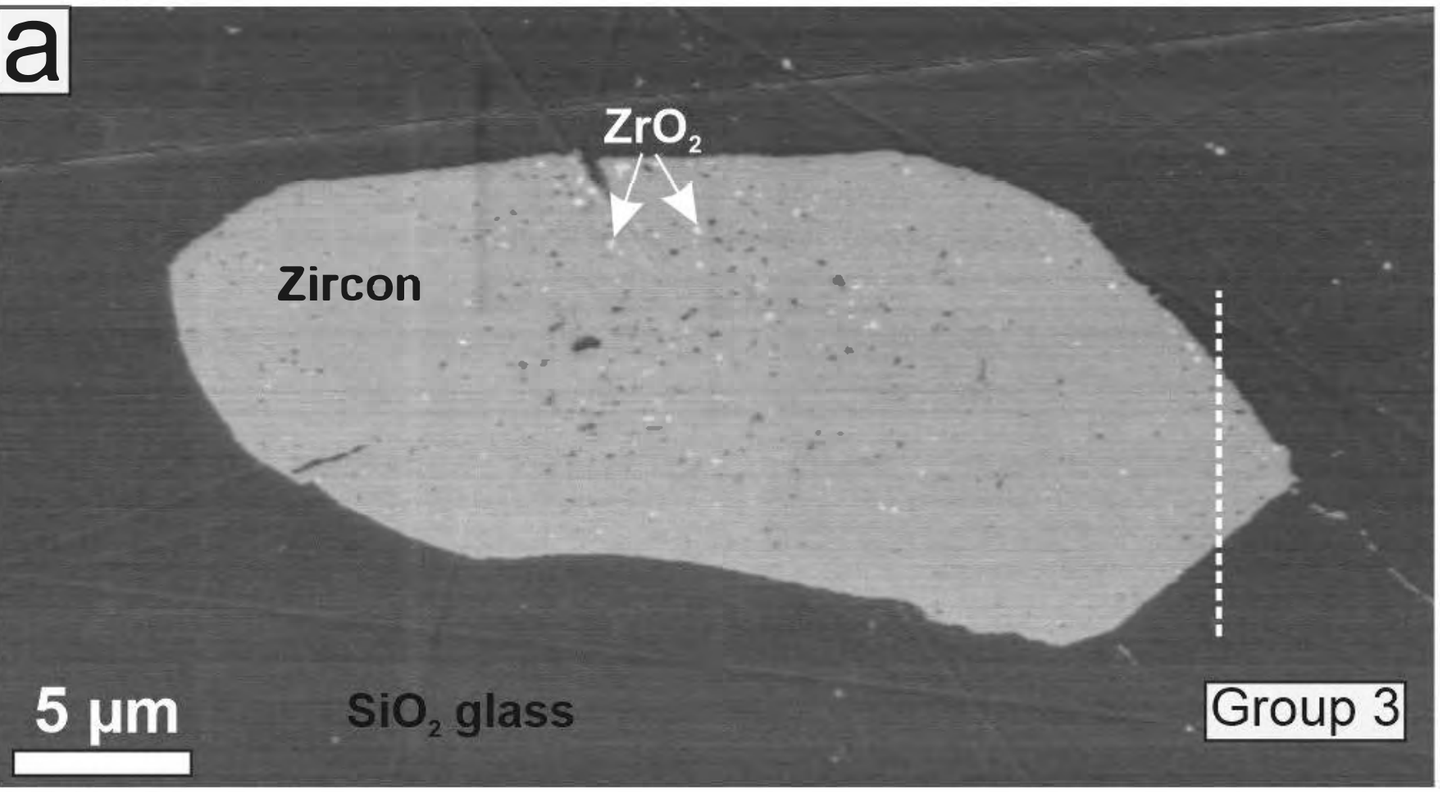
a
$ZrO_2$
Zircon
5 µm
$SiO_2$ glass
Group 3

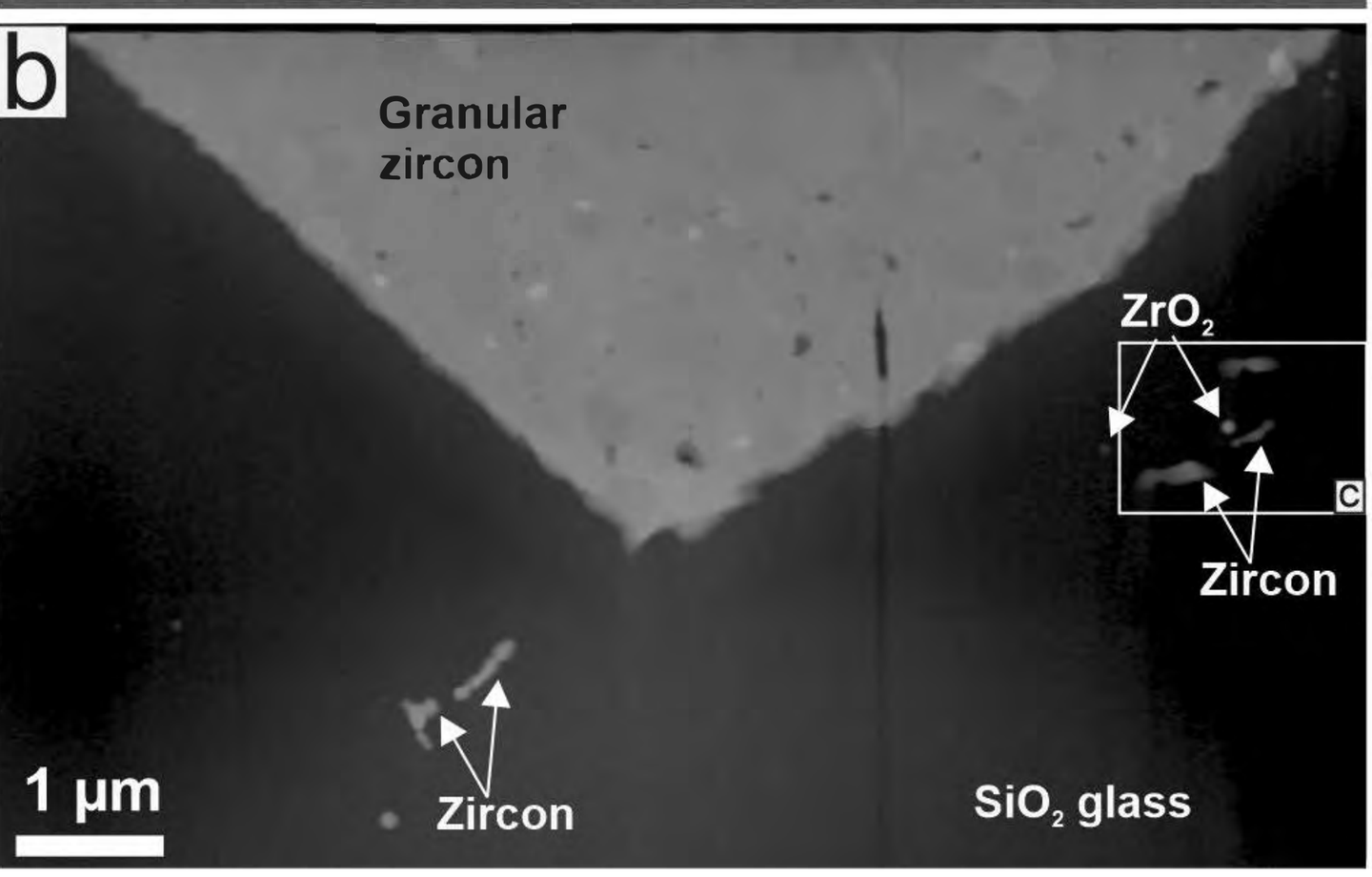
b
Granular
zircon
$ZrO_2$
C
Zircon
1 µm
Zircon
$SiO_2$ glass

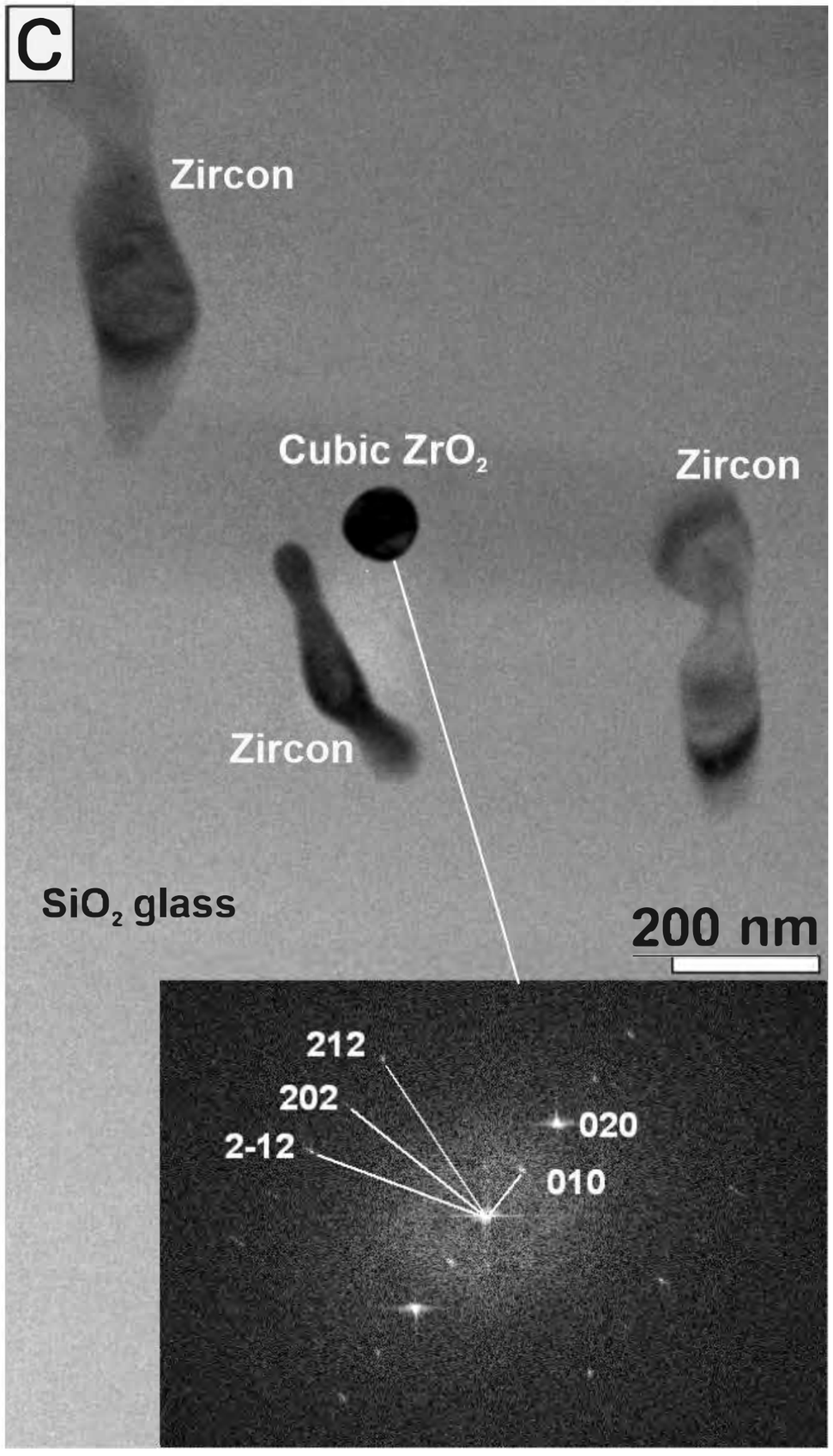
c
Zircon
Cubic $ZrO_2$
Zircon
Zircon
$SiO_2$ glass
200 nm
212
202
2-12
020
010

# Figure 8

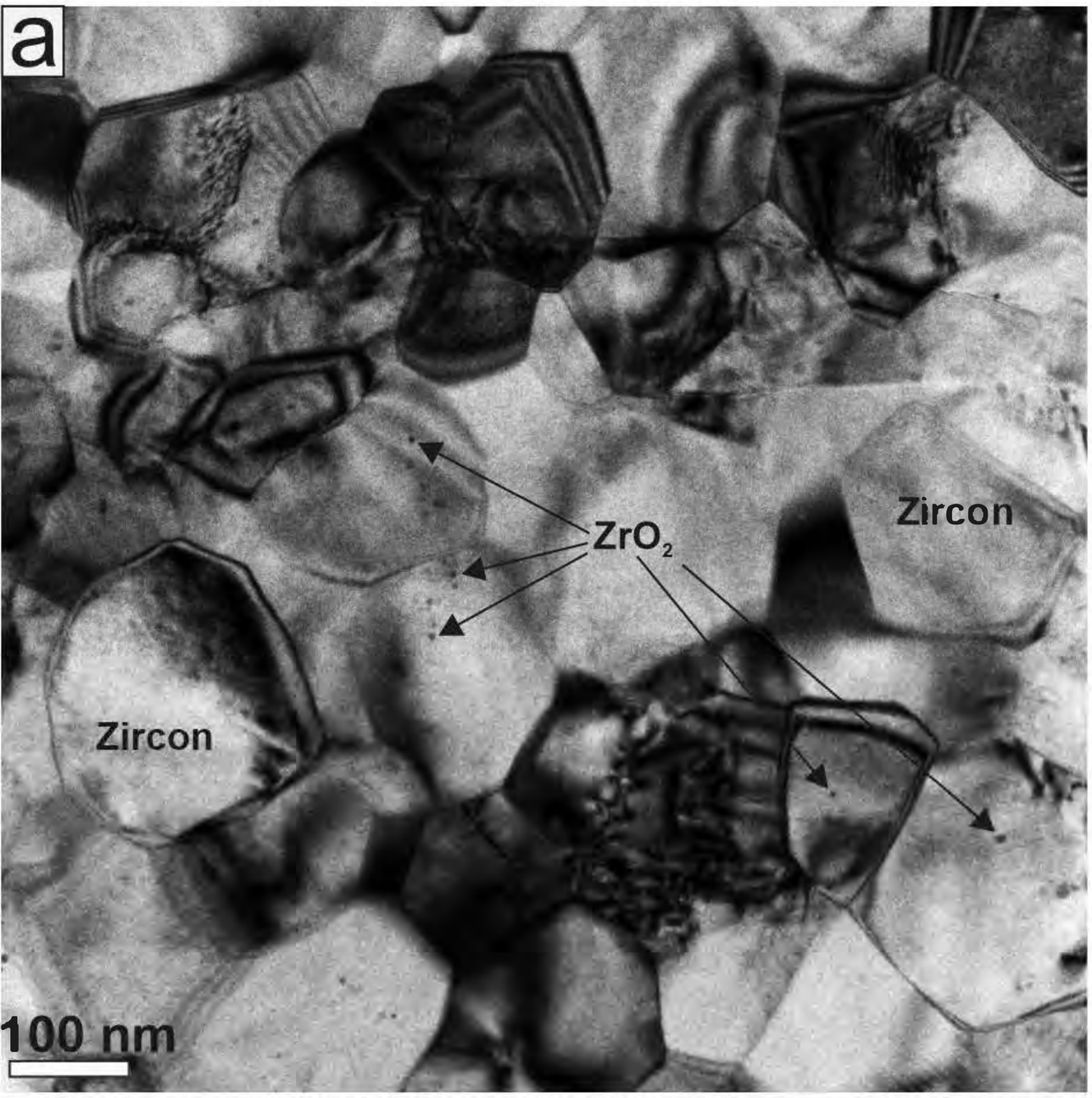


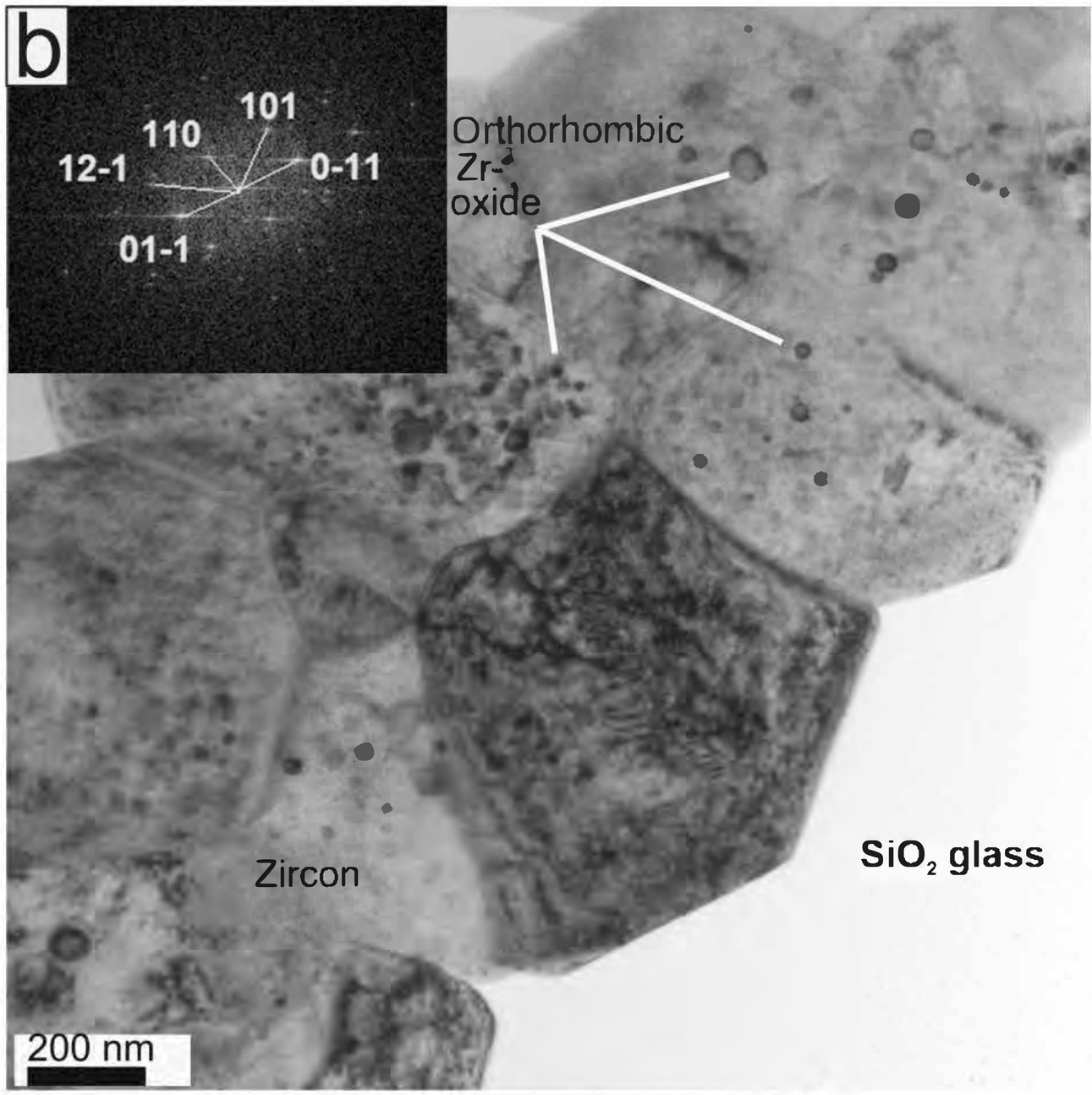


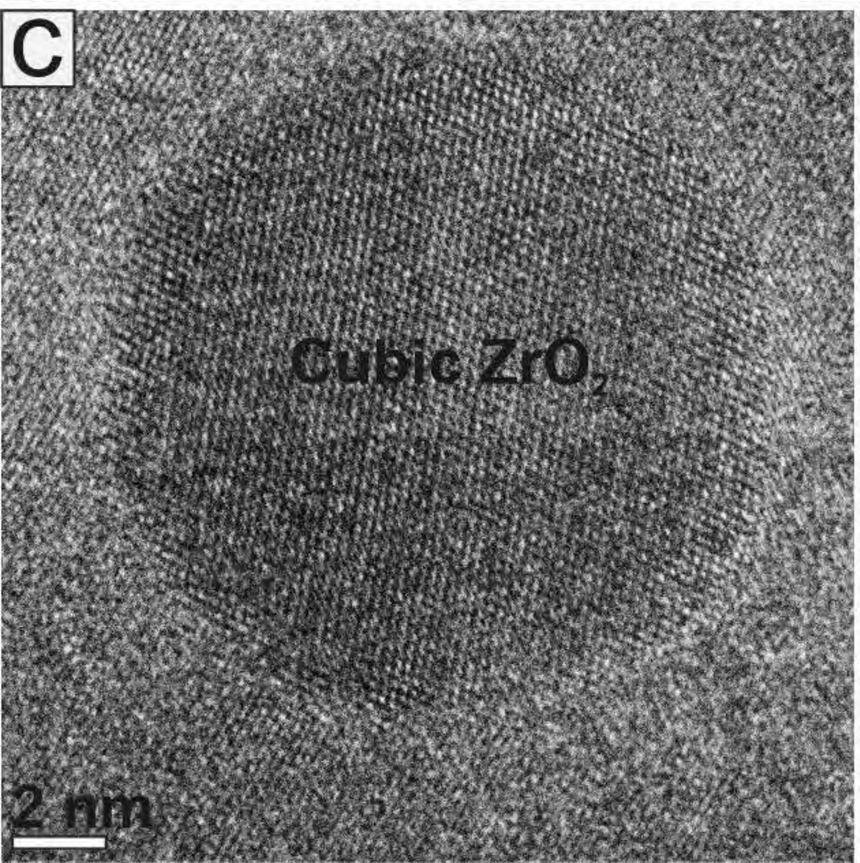


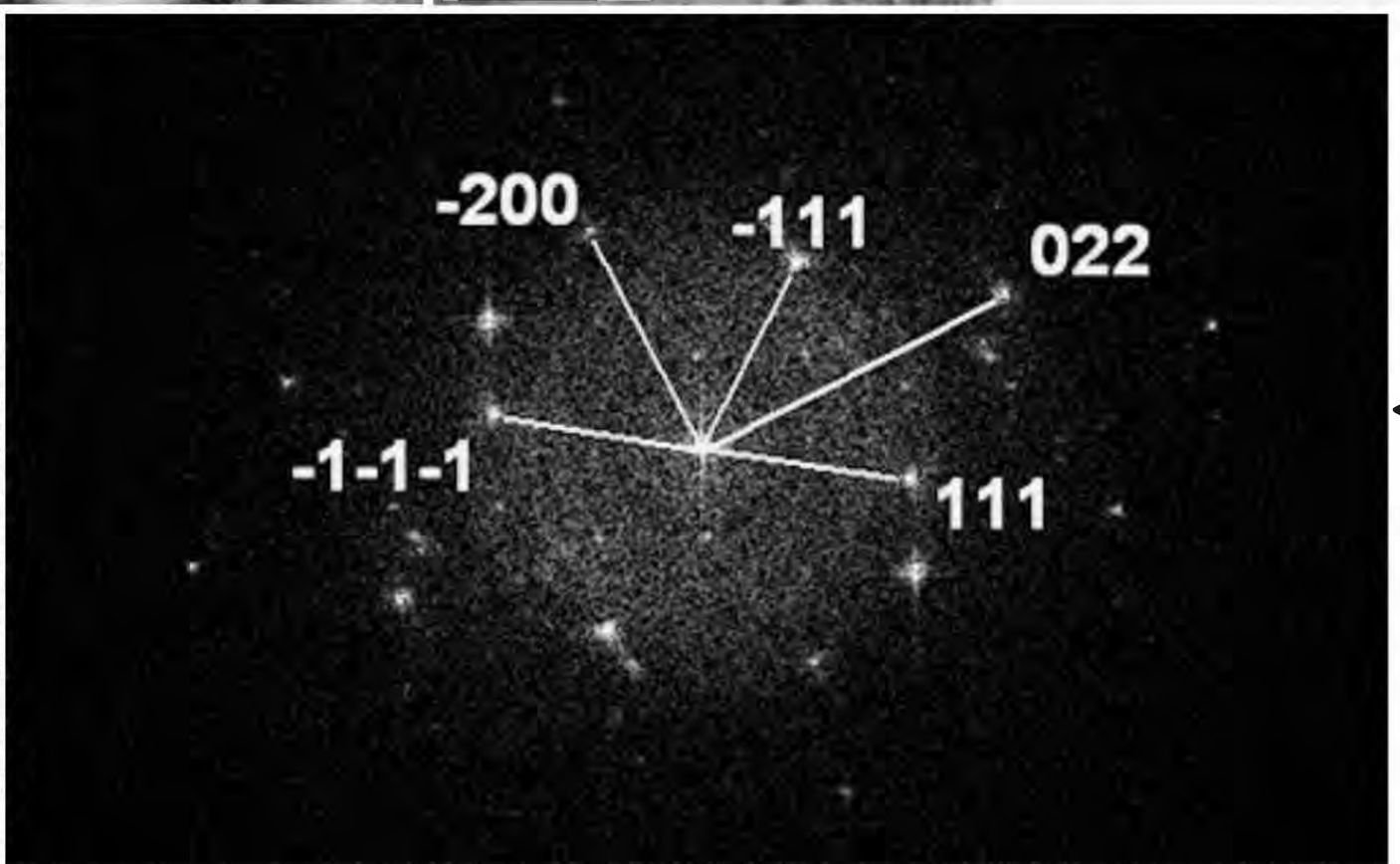


◄ Cubic zirconia

# Figure 9

a

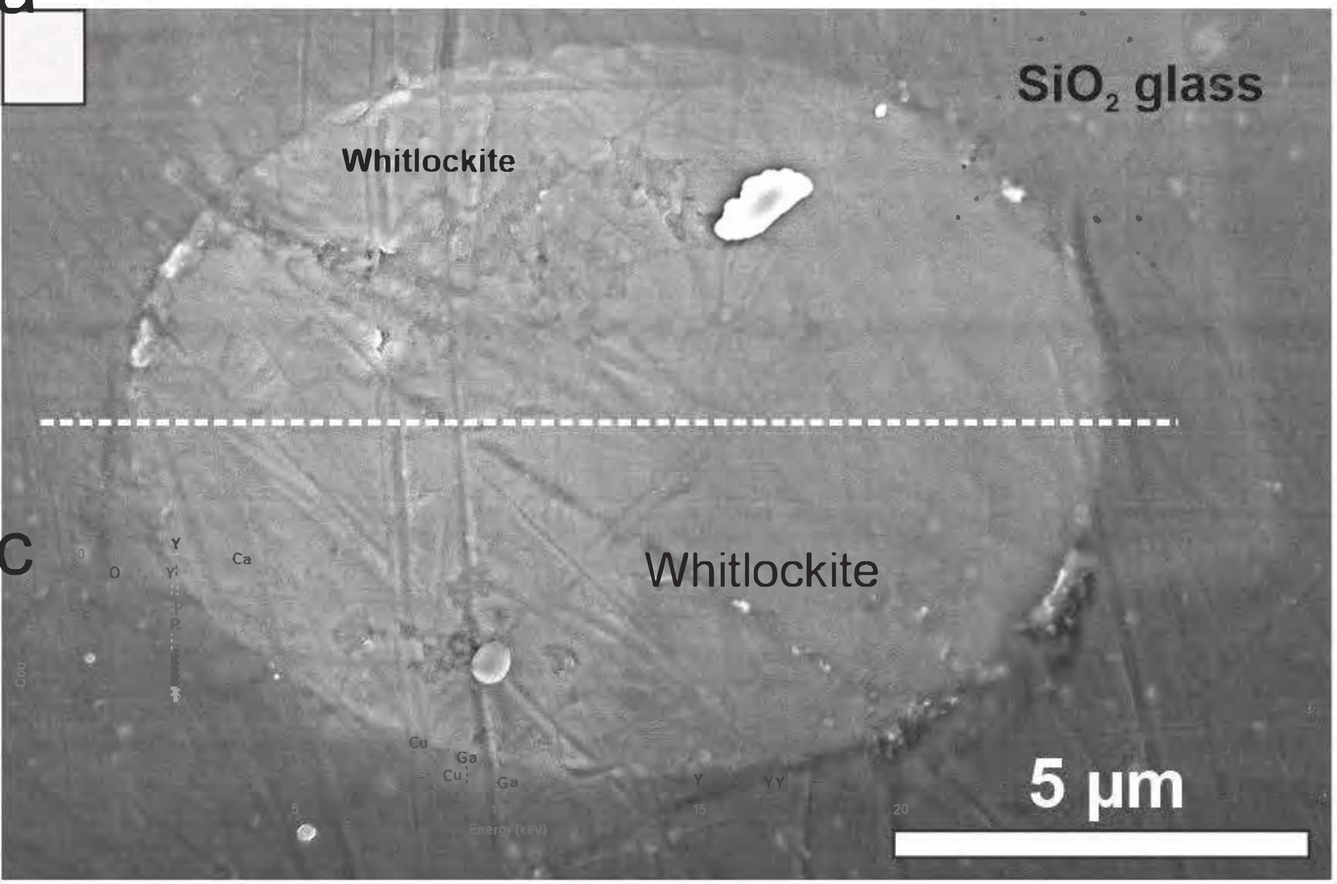


b

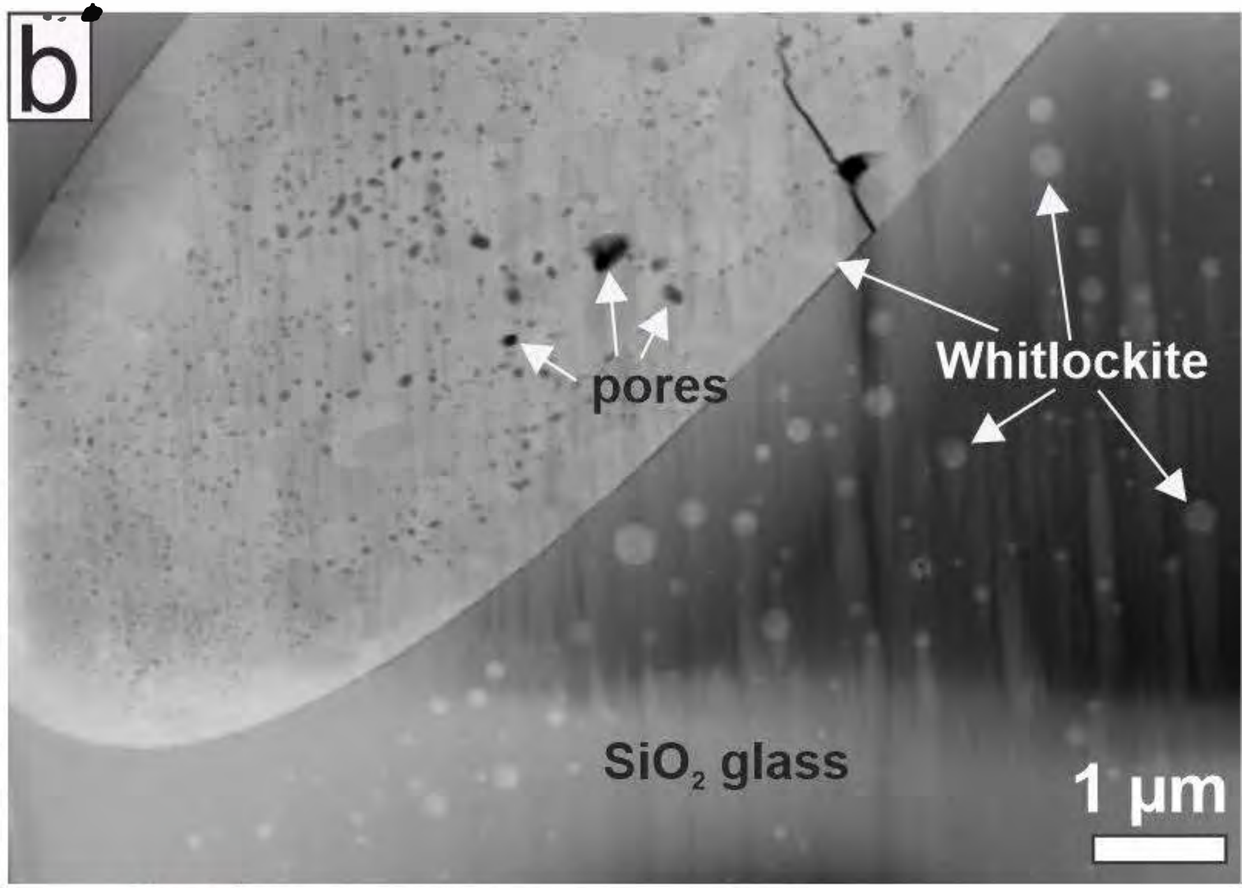


c

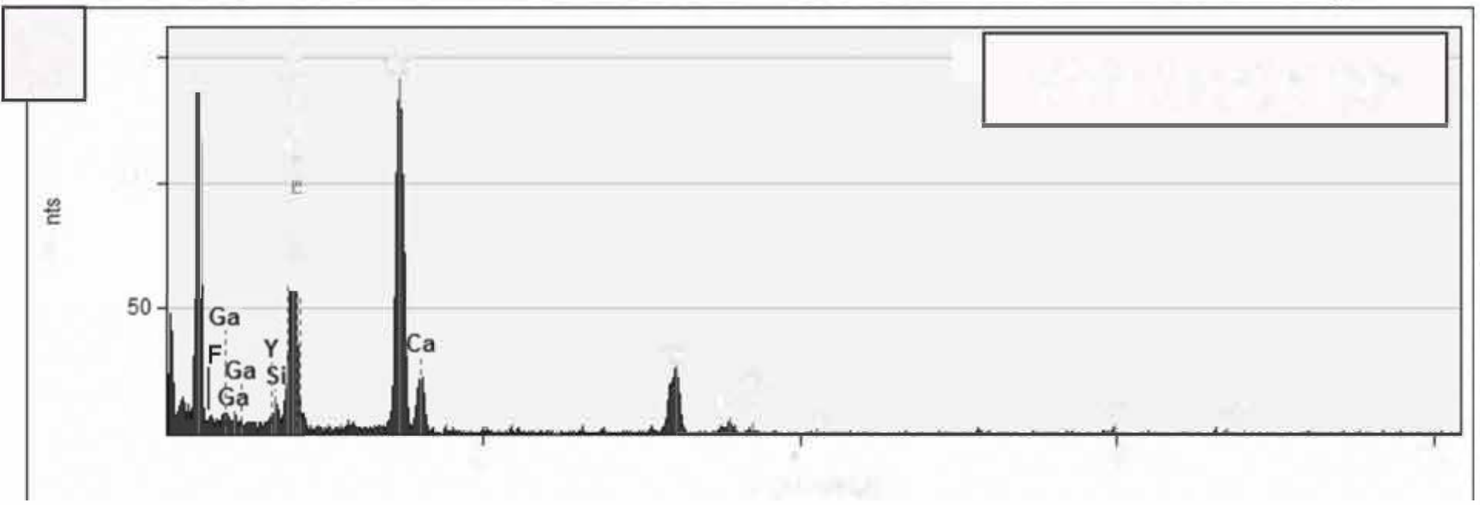


d

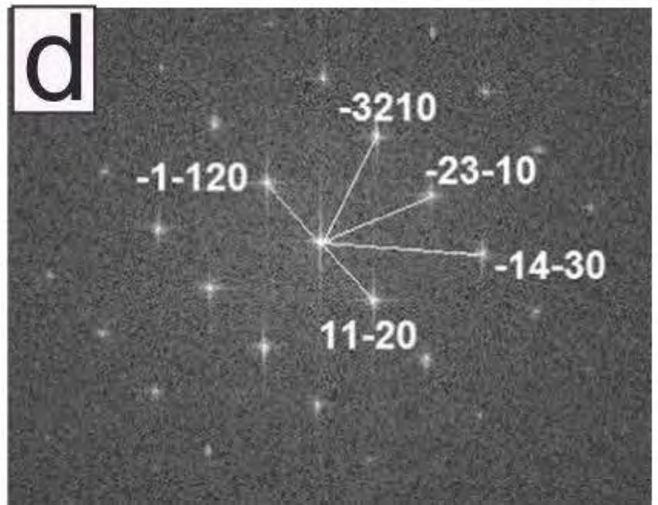


◄ Whitlockite

# Figure 10

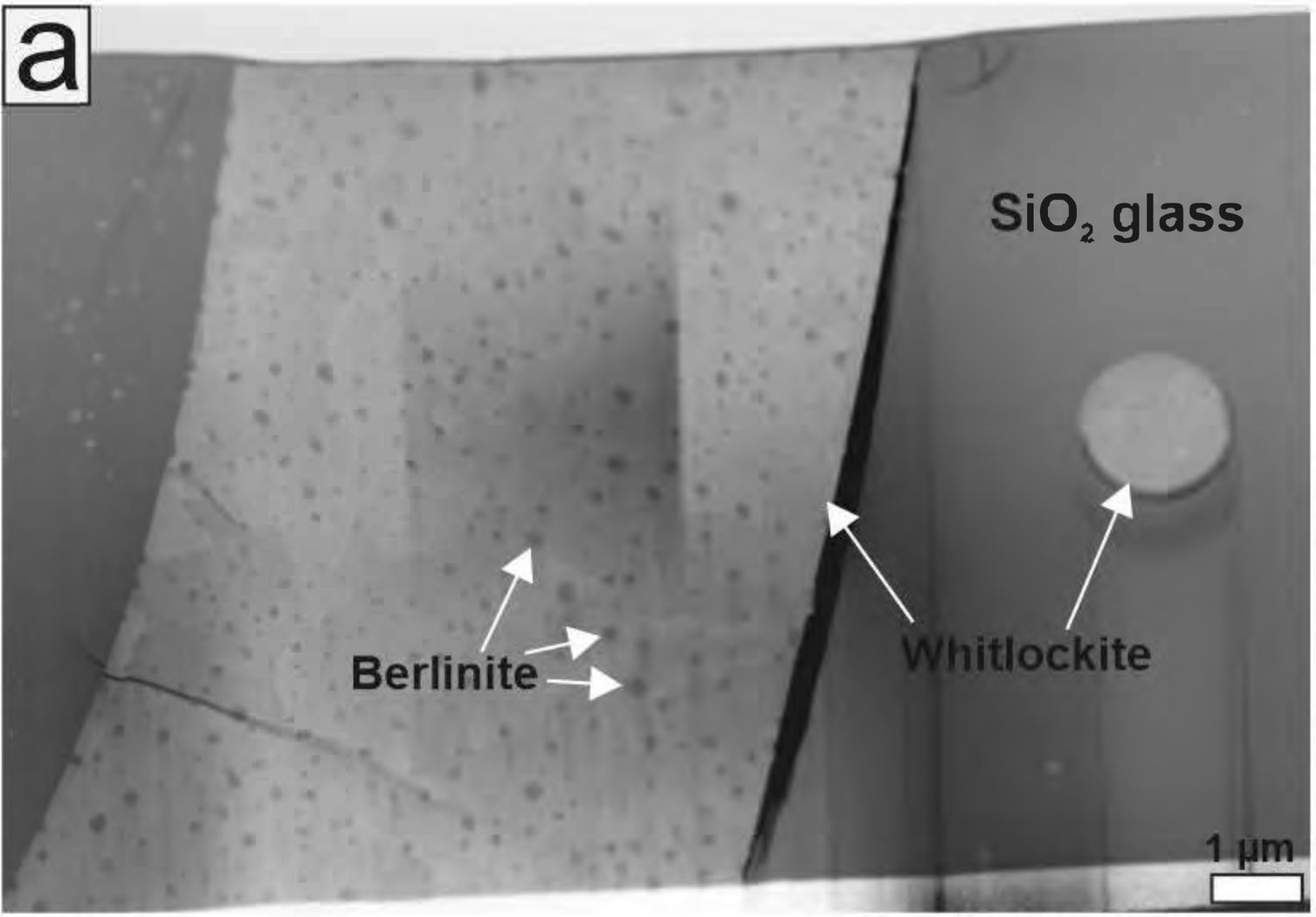


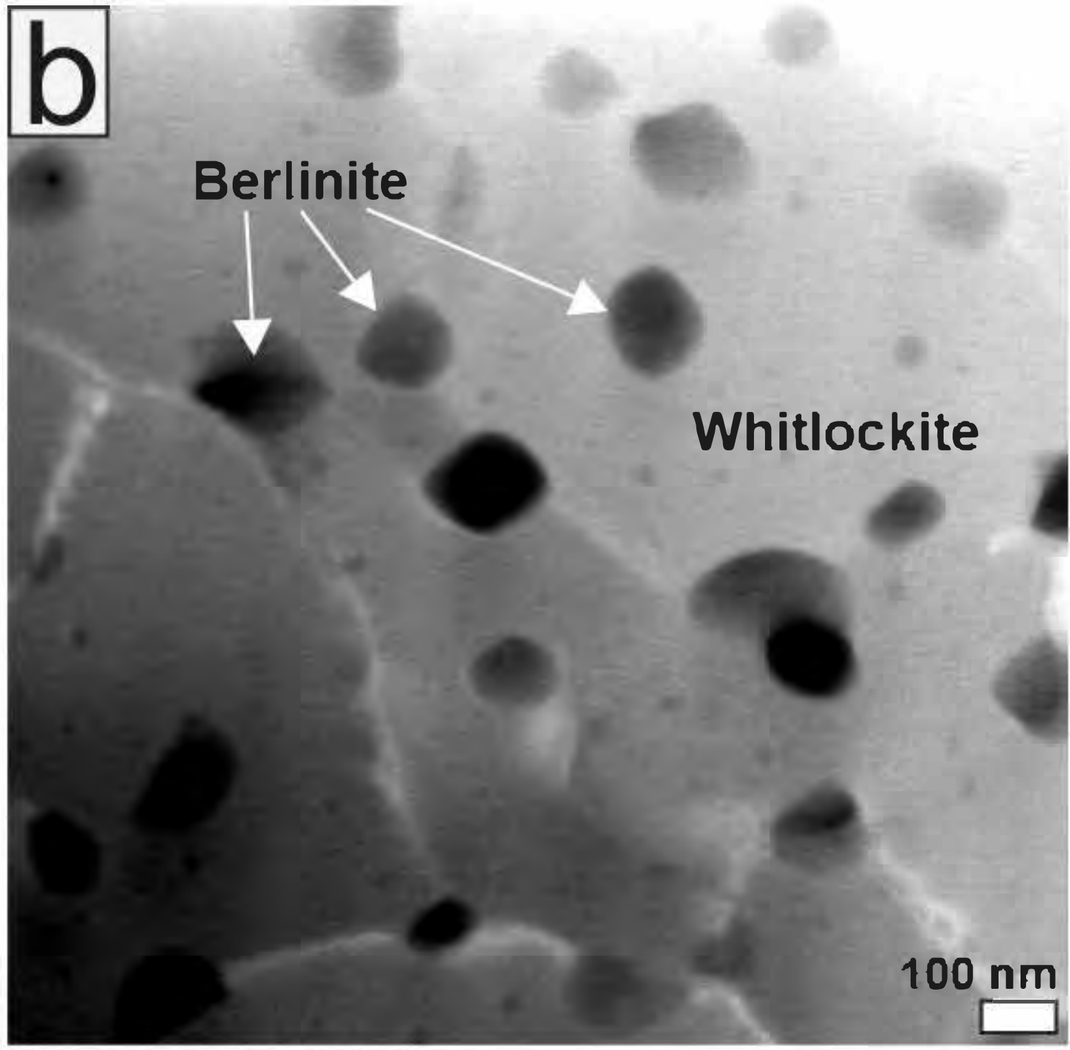


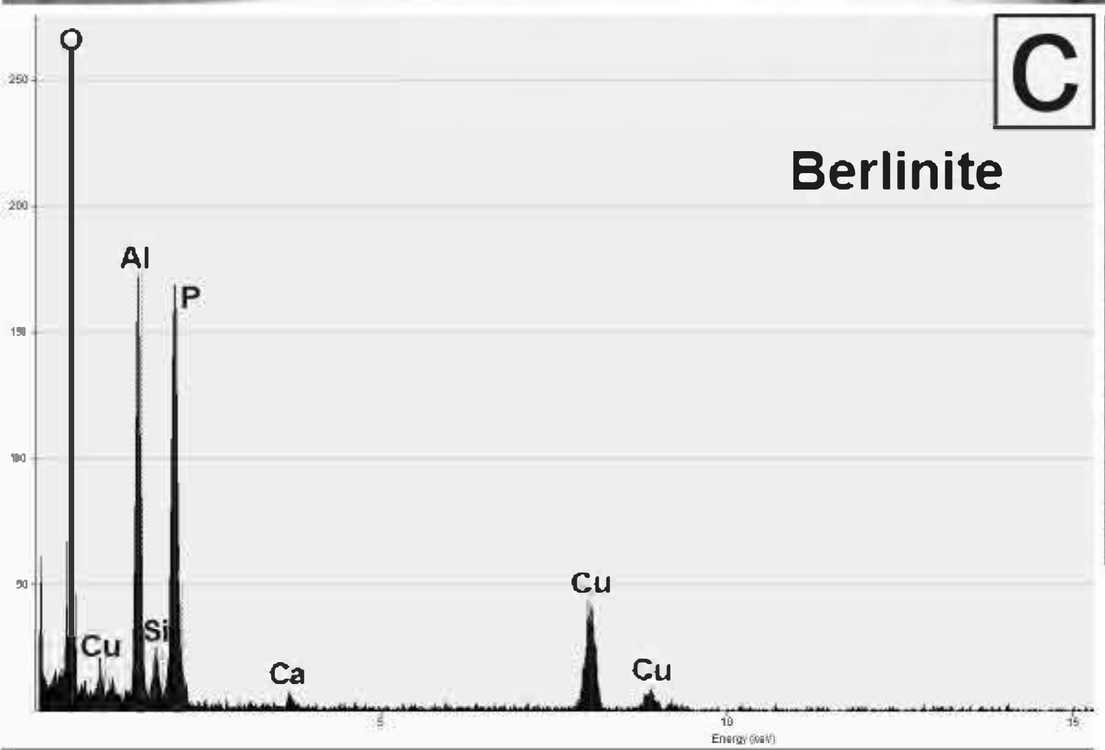


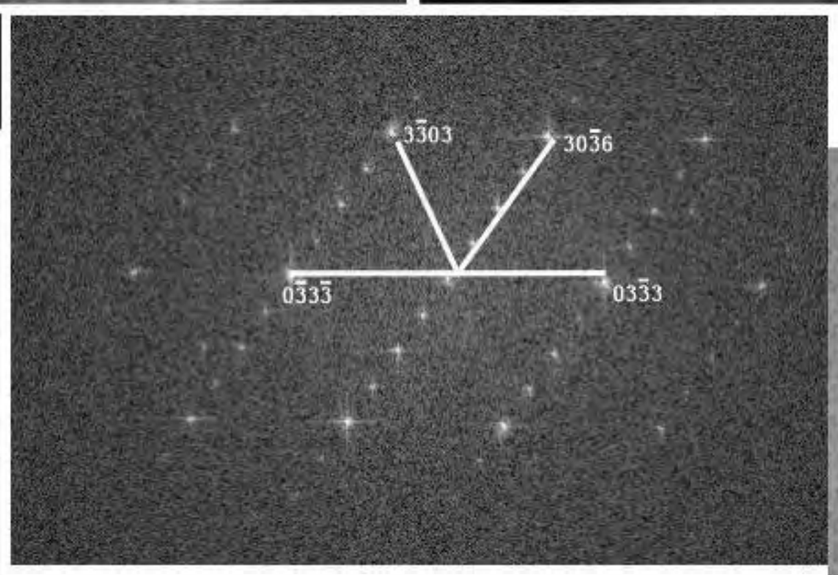


▲ Whitlockite

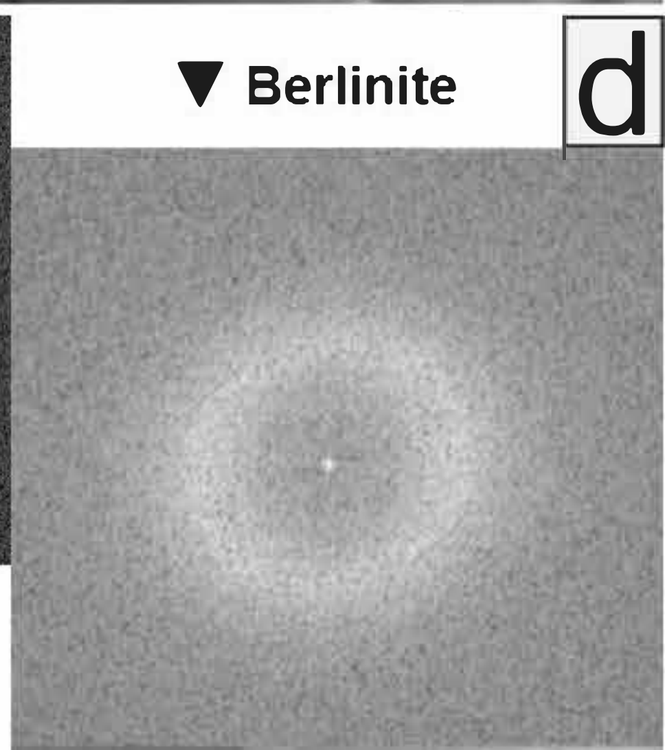

# Figure 11

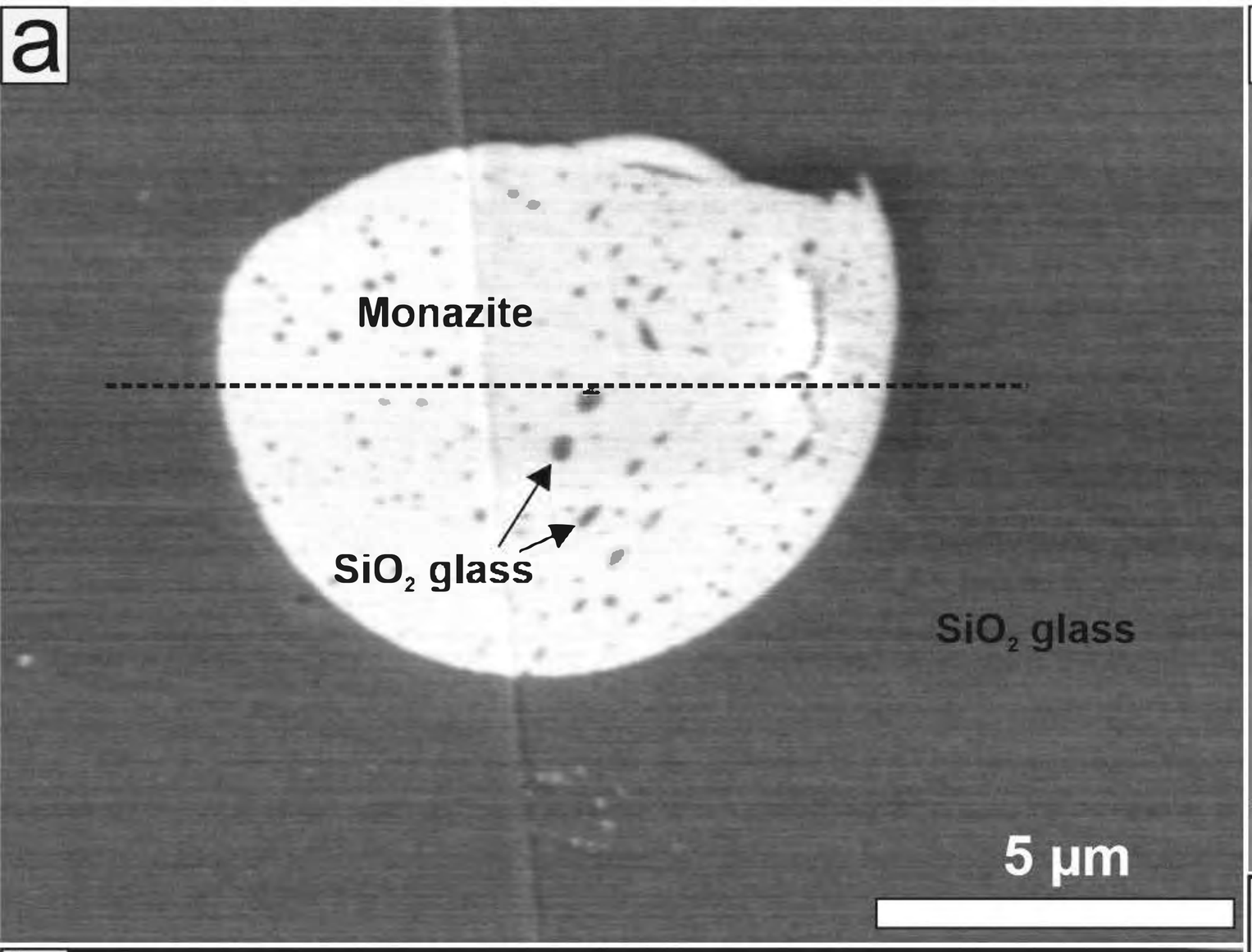
a
Monazite
SiO2 glass
SiO2 glass
5 µm

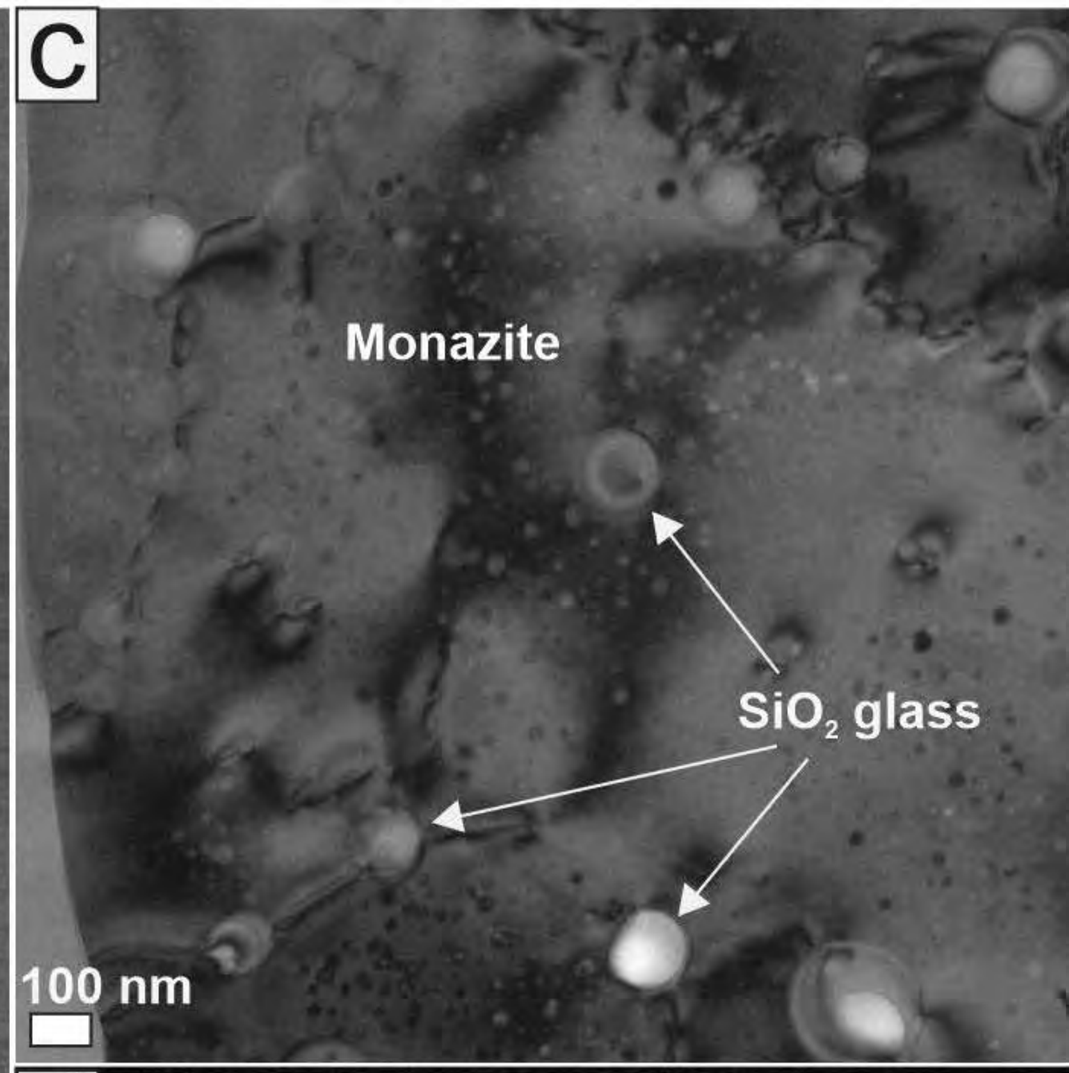
c
Monazite
SiO2 glass
100 nm

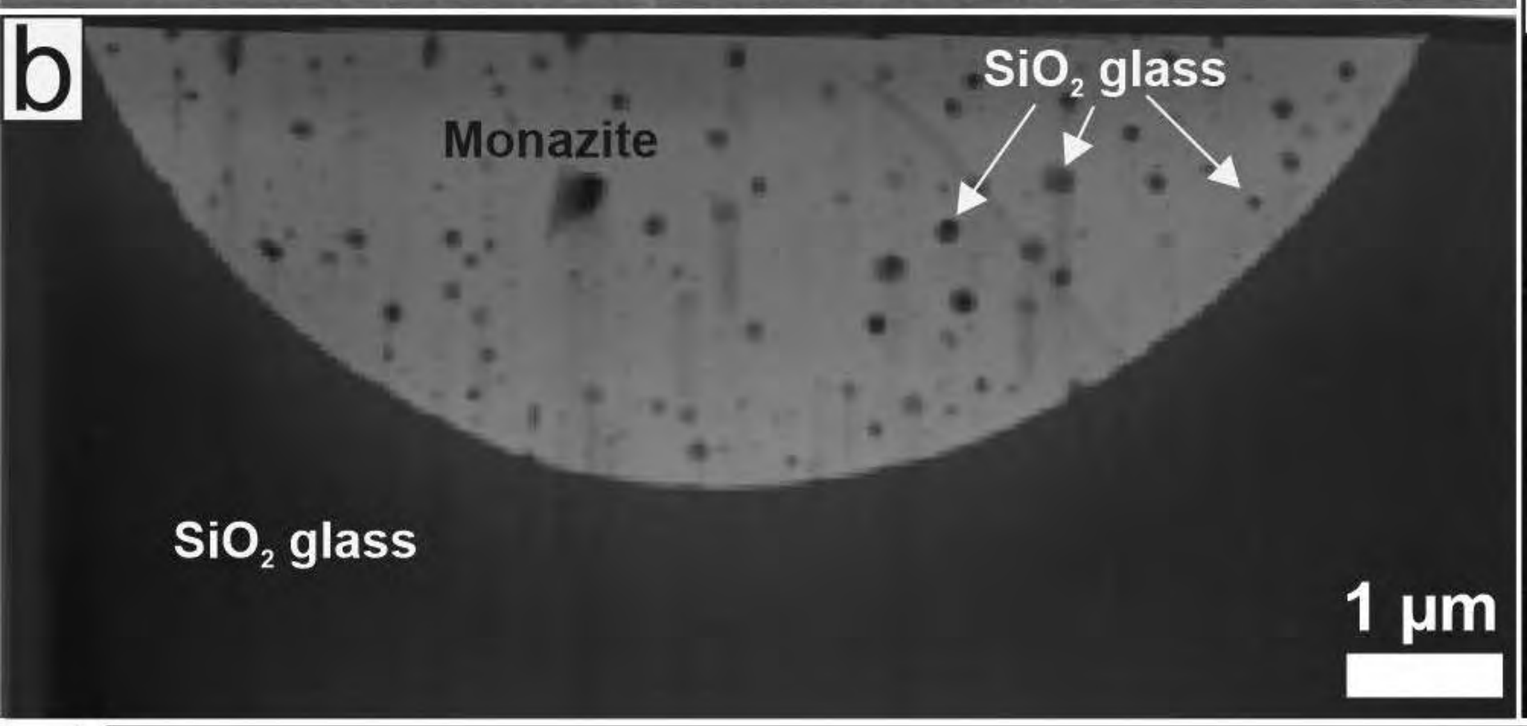
b
Monazite
SiO2 glass
SiO2 glass
1 µm

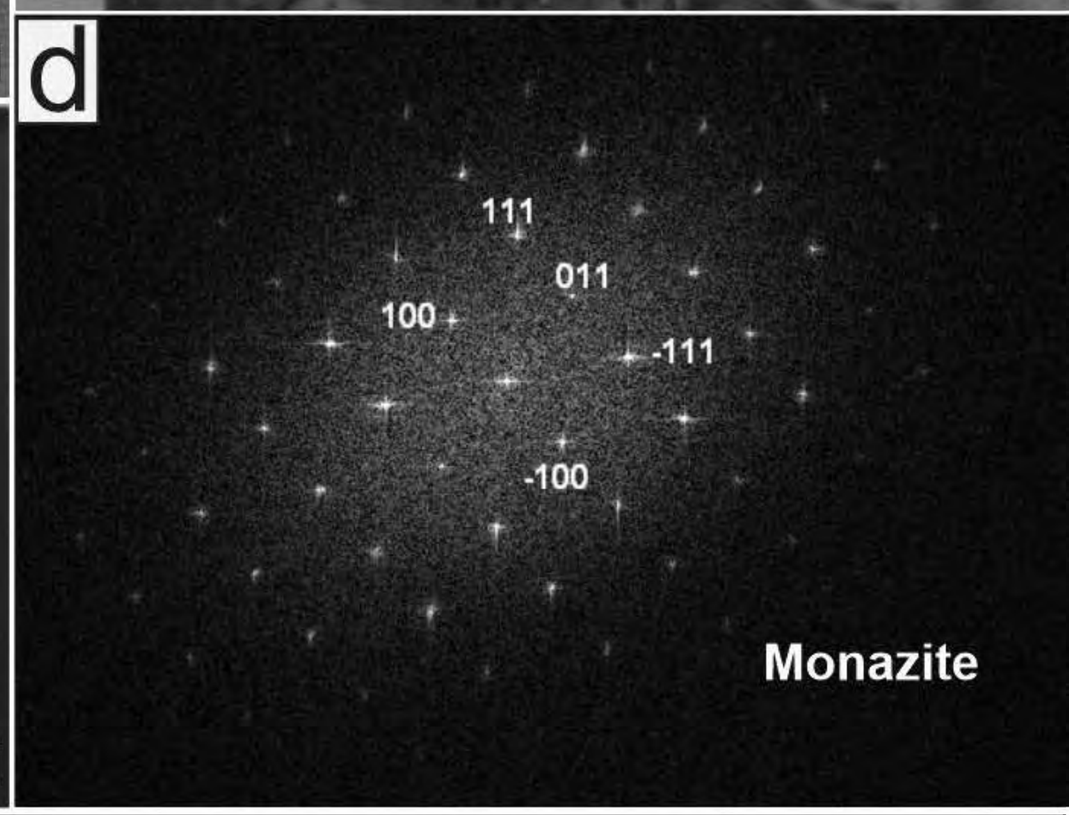
d
111
011
100
-111
-100
Monazite

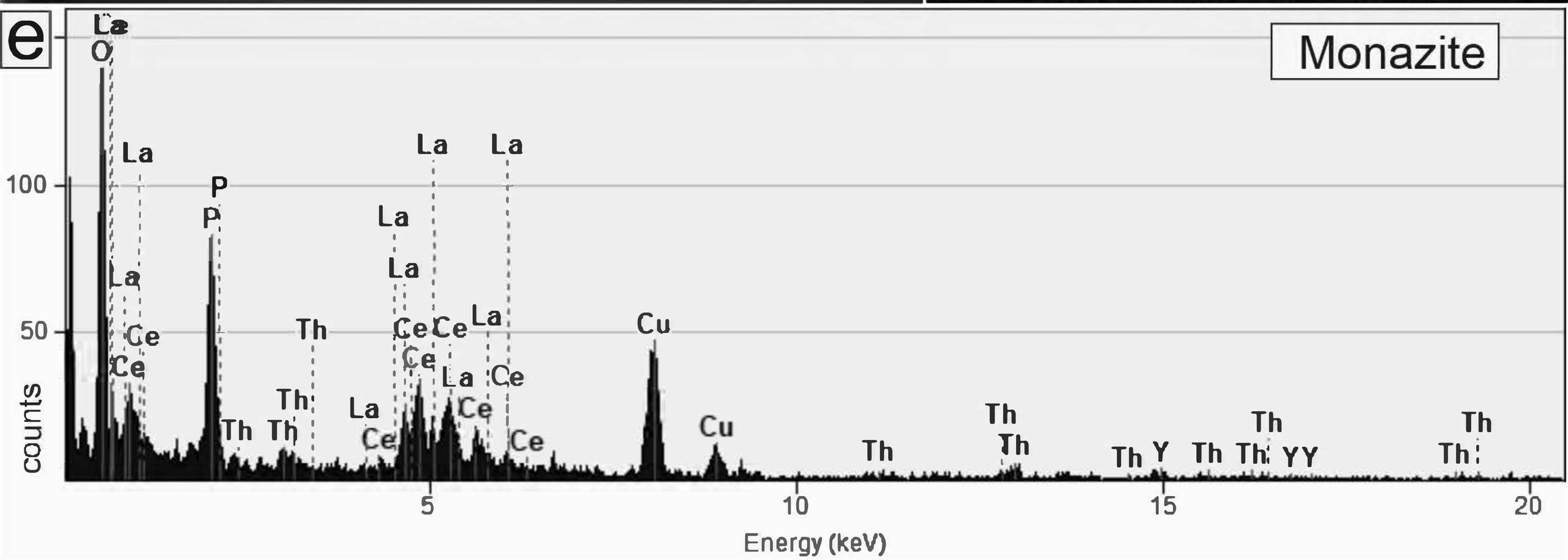
e
Monazite
counts
Energy (keV)
100
50
5
10
15
20
La
O
La
P
P
La
Ce
Ce
Th
Th
Th
La
Ce
La
La
Ce
Ce
Ce
La
La
Ce
Ce
Cu
Cu
Th
Th
Th
Th
Y
Th
Th
YY
Th
Th

# Figure 12

| $ZrO_2$ polymorph | Space group | $a_0$ | $b_0$ | $c_0$ | α | β | γ |
|---|---|---|---|---|---|---|---|
| Baddeleyite (monoclinic) | P 1 21/c 1 | 5.1827 Å | 5.21168 Å | 5.3731 Å | 90° | 98.83° | 90° |
| Tetragonal | P 42/n m c Z | 3.6358 Å | 3.6358 Å | 5.2257 Å | 90° | 90° | 90° |
| Cubic | F m -3 m | 5.1291 Å | 5.1291 Å | 5.1291 Å | 90° | 90° | 90° |
| Orthorhombic | P n a m | 5.5873 Å | 6.4847 Å | 3.3298 Å | 90° | 90° | 90° |

Table 1. Lattice cell parameters of various polymorphs of $ZrO_2$ that were used to identify the phases (Boysen et al. 1991, monoclinic; Martin et al. 1993, tetragonal and cubic; Haines et al. 1995, 1997, orthorhombic).

| Analyzed image | Measured d-spacing (Å) | Calculated (theoretical) d-spacing (Å) | Corresponding lattice plane | Two adjacent planes | Measured angle (°) | Calculated (theoretical) angle (°) |
|---|---|---|---|---|---|---|
| FFT of HREM09 | 6.76 | 6.484 | (010) | 011\|001 | 24 | 27.18 |
| | 3.06 | 3.3298 | (001) | 011\|010 | 63.5 | 62.82 |
| | 2.88 | 2.962 | (011) | 0 $\bar{1}$ 1\|001 | 26 | 27.18 |
| | 2.75 | 2.962 | (011) | 0 $\bar{1}$ 1\|010 | 66 | 62.82 |
| FFT of HREM10 | 4.63 | 4.2325 | (110) | 101\|110 | 68.6 | 67.18 |
| | 3.13 | 2.962 | (011) | 101\|0 $\bar{1}$ 1 | 39 | 40.17 |
| | 3.05 | 2.8603 | (101) | 12 $\bar{1}$ \|110 | 45 | 43.72 |
| | 2.24 | 2.1449 | (12 $\bar{1}$) | 12 $\bar{1}$ \|01$\bar{1}$ | 28 | 28.93 |

Table 2. Lattice cell parameters of orthorhombic OII $ZrO_2$ polymorph, measured vs. theoretical after Haines et al. (1995, 1997).